

Article

Geological and Geochemical Characteristics of the Archean Basement-Hosted Gold Deposit in Pinglidian, Jiaodong Peninsula, Eastern China: Constraints on Auriferous Quartz-Vein Exploration

Ruihong Li ^{1,2,*}, Ntwali Ntabira Albert ¹, Menghe Yun ¹, Yinsheng Meng ² and Hao Du ³

¹ State Key Laboratory of Geological Processes and Mineral Resources, China University of Geosciences, Beijing 100083, China; albertntnt@163.com (N.N.A.); ymmmmh@163.com (M.Y.)

² Institute of Geophysical and Geochemical Exploration, Chinese Academy of Geological Sciences, Langfang 065000, China; mengyinsheng@igge.cn

³ Sanshandao Gold Company, Shandong Gold Mining Stock Co., Ltd., Laizhou 261438, China; duhaouu@163.com

* Correspondence: liruihong@igge.cn; Tel.: +86-(0316)-2267628

Received: 18 December 2018; Accepted: 16 January 2019; Published: 21 January 2019



Abstract: The gold deposits that are hosted in the Archean metamorphic rock, have yet to be explored beyond Pinglidian gold deposit in the northwestern Jiaodong Peninsula, eastern China. This kind of gold deposit differs from those that are hosted in Mesozoic granitoids, showing good potential for the prospecting of auriferous quartz-vein gold deposits controlled by the structures in greenfield Archean metamorphic rock. Pinglidian gold deposit is located in the hanging wall of the Jiaojia fault and consists of eight separated orebodies that are enveloped by altered rock in Archean biotite plagiogneiss. These orebodies and wall-rock alterations are strongly controlled by local structures that formed during the Mesozoic rotation and kink folding of the foliated and fissile Archean basement host. The major wall-rock alterations comprise sericitization, silicification, pyritization, and carbonation, which is up to 18 m in width and progressively increases in intensity towards the auriferous quartz vein. The visible gold is present as discrete native gold and electrum grains, which have basically filled in all manner of fractures or are adjacent to galena. We recognize two types of gold bearing quartz veins that are associated with mineral paragenetic sequences during hydrothermal alteration in the Pinglidian gold deposit. The petrological features and geochemical compositions in the reaction fronts of the alteration zone suggest variations in the physicochemical conditions during ore formation. These minerals in the wall rock, such as plagioclase, biotite, zircon, titanite, and magnetite, have been broken down to hydrothermal albite, sericite, and quartz in a K–Na–Al–Si–O–H system, and sulfides in a Fe–S–O–H system. The major and trace elements were calculated by the mass-balance method, showing gains during early alteration and losses during late alteration. The contents of K₂O, Na₂O, CaO, and LOI varied within the K–Na–Al–Si–O–H system during alteration, while Fe₂O₃ and MgO were relatively stable. Rare-earth elements (REE) changed from gains to losses alongside the breakdown of accessory minerals, such as large ion lithophile elements (LILE). The Sr and Ba contents exhibited high mobility during sericite-quartz alteration. Most of the low-mobility high-field strength elements (HFSE) were moderately depleted, except for Pb, which was extremely high in anomalous samples. The behavior of trans-transition elements (TRTE) was related to complicated sulfides in the Fe–S–O–H system and was constrained by the parameters of the mineral assemblages and geochemical compositions, temperature, pressure, pH, and *f*O₂. These factors during ore formation that were associated with the extents and intensity of sulfide alteration and gold precipitation can be utilized to evaluate the potential size and scale of an ore-forming hydrothermal system, and is an effective exploration tool for widespread auriferous quartz veins in Archean metamorphic basements.

Keywords: Archean basement; quartz vein; hydrothermal alteration halo; Pingliidian gold deposit; Jiaodong

1. Introduction

The Precambrian terrane over the globe are important repositories of major gold deposits [1]. However, many of the world-class gold deposits in the North China Craton (NCC) are spatially associated with Mesozoic magmatic intrusions and related processes in Jiaodong [2–4], and their formation has been correlated with massive hydrothermal alterations [5–7]. Hydrothermal alterations are traditionally prevalent in the upper crust, especially in regional-scale fault zones, including K-feldspathization, albitization, silicification, sericitization, carbonatization, chloritization, and sulfidation [8–13]. Mesothermal gold deposits typically form during compressional or transpressional tectonic events [14,15], wherein regional-scale alteration requires abundant fluid and mass transport through channels by the reactivation of previous faults or hydrofractures [16,17]. However, the occurrence of large auriferous quartz veins and hydrothermal halos in low-permeability Archean metamorphic rocks results from the diffusive metasomatism of wall rock, invoking extremely large fluid fluxes and dense brittle microfracture pathways [18,19]. When the fluid contacts mineral assemblages in wall rock, the system is immediately no longer in equilibrium, and re-equilibration reactions in the presence of a fluid phase drive large-scale processes, such as dissolution and precipitation [20]. Thus, the formation and development of products, such as alteration halos and quartz veins, are related to fluid-rock interactions and mass transport, which strongly affect the petrology and geochemical composition of the original rock [21]. Numerous field evidence and experimental observations indicated that fluid-induced reaction fronts migrate from veins to fresh wall rock through pores or microfractures [12,20,22]. Metamorphism that is accompanied by a change in the rock composition is referred to as metasomatism and is normally assumed to be the response to fluid-controlled mass transfer rather than purely to changes in P–T conditions [23,24]. Accordingly, large-scale hydrothermal alteration zones depend on the development and maintenance of an efficient porosity-permeability system during fluid-rock interactions in natural rocks [25], emphasizing the importance of mineral-assemblage replacement reactions during ore formation.

Jiaodong Peninsula is the most important gold province in the NCC [13,26,27]. The majority of the gold resources (>95%) are hosted in Mesozoic granitoids and are currently recognized as one of the largest granitoid-hosted gold provinces in the world [9]. These gold deposits are generally classified as disseminated-/stockwork-type (Jiaojia-type) and auriferous quartz-vein-type (Linglong-type) deposits, and both are hosted in Mesozoic granitoids and prominently controlled by regional-scale NE- to NNE-trending fault zones (Figure 1) [13,28–32]. Li et al. detailed the significant alteration halos that envelop the low-grade disseminated-/stockwork-type ore [12], however, high-grade auriferous quartz vein-type ores have traditionally been conceptualized to have negligible wall-rock alteration. Recognizing such alteration zones increases the target mineralized zone and the volume of potential ore during exploration [10,33]. Actually, the original mineral assemblages and structure-controlled fluid flow are obscured by alteration reactions in centimeter- to decameter-scale alteration zones in Mesozoic granitoids. Meanwhile, the detailed hydrothermal alteration of host rocks, especially Precambrian metamorphic rock instead of Mesozoic rock in auriferous quartz-vein gold deposits, has rarely been described.

In this paper, we begin with observations at the underground-outcrop scale and then carefully examine changing mineral assemblages and textural relationships in thin sections, and conduct whole-rock geochemistry analysis and electron microprobe analysis on sulfides to interpret the ore formation in the hydrothermal alteration halos in the Pingliidian gold deposit in Archean metamorphic rock, instead of the well-known Mesozoic granitoids in Jiaodong.

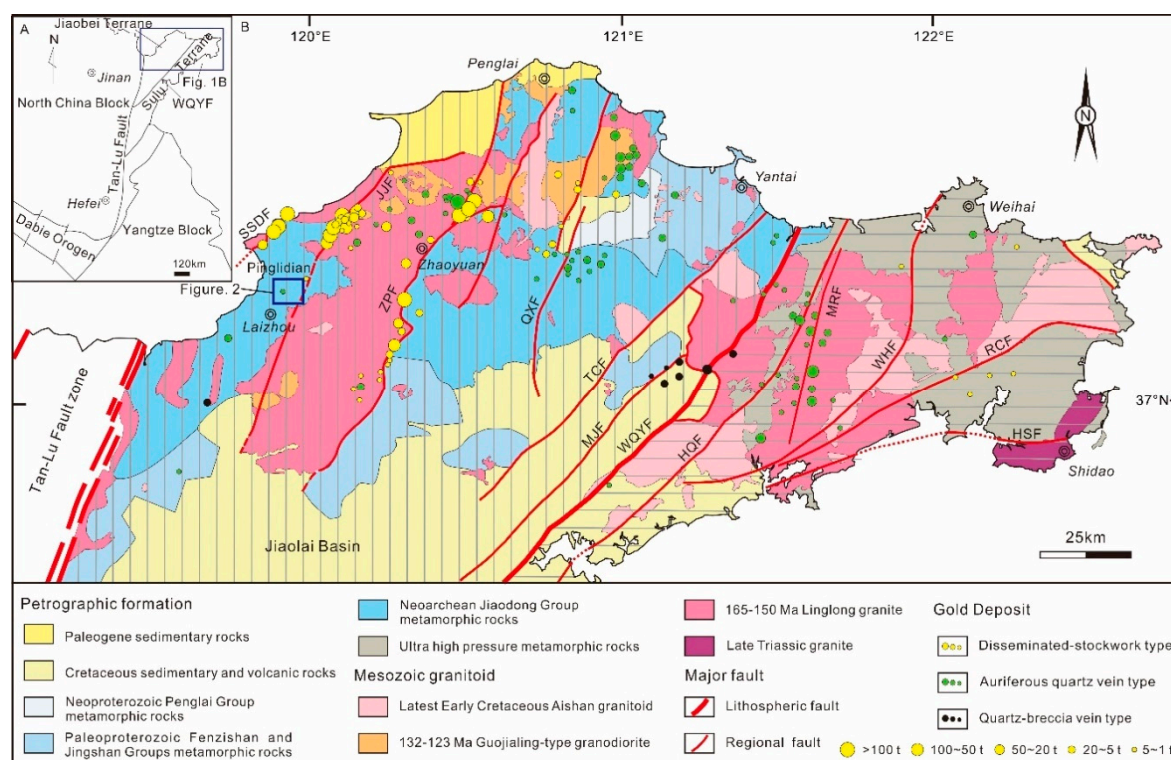


Figure 1. (A) Simplified tectonic map of the Jiaodong Peninsula. (B) Geological map of the Jiaodong gold province, showing the distribution of major fault zones, Precambrian metamorphic rocks, Mesozoic granitoid intrusions, sedimentary rocks, and gold deposits [26]. The different circle sizes represent five tonnage ranges for the gold deposits (>100 t, 100–50 t, 50–20 t, 20–5 t, and 5–1 t). The Jiaojia goldfield is situated in the northwestern Jiaodong Peninsula. HQF, Haiyang–Qingdao Fault; HSF, Haiyang–Shidao Fault; JJF, Jiaojia Fault; MJF, Muping–Jimo Fault; MRF, Muping–Rushan Fault; QXF, Qixia Fault; RCF, Rongcheng Fault; SSDF, Sanshandao Fault; TCF, Taocun Fault; WHF, Weihai Fault; WQYF, Wulian–Qingdao–Yantai Fault; ZPF, Zhaoping Fault.

2. Regional Geology

The Jiaodong Peninsula occupies the southeastern corner of the North China Block (NCB) and the northeastern corner of the South China block (SCB) [7,9,12,34]. These two blocks are separated by the Wulian–Qingdao–Yantai Fault (WQYF), associated with the Triassic collisional event [26]. The northwestern area of Jiaodong is called the Jiaobei Terrane, and the southeastern area is called the Sulu Terrane. The Jiaobei Terrane was divided into the Jiaobei uplift to the north and the Jiaolai Basin to the south by an E–W-trending normal fault during Early Cretaceous [35]. The Jiaobei uplift consists of Precambrian metamorphic basement and Mesozoic intrusions. More than 95% of the gold resources in the Jiaodong Peninsula are hosted by Late Jurassic and Early Cretaceous granitoids (Figure 1) [5,12]. Most of the gold deposits are controlled by NE- to NNE-trending fault systems, with a spacing of approximately 15–30 km from west to east (Figure 1) [36].

The Precambrian metamorphic basement is dominated by Mesoarchean to Neoarchean trondhjemite-tonalite-granodiorite (TTG) gneisses [37,38], Neoarchean Jiaodong Group metamorphic rocks, and Paleoproterozoic Fenzishan and Jingshan Group metamorphic rocks, which occupy approximately half of the northwestern Jiaodong Peninsula (Figures 1 and 2) [39,40]. The Jiaodong Group metamorphic rocks consist of biotite plagiogneiss, biotite granulite, amphibolite, and biotite-hornblende-plagioclase gneiss [41]. The Fenzishan Group is a Proterozoic high-grade metasedimentary sequence of calc-silicate rocks, marble, and minor amphibolite [42]. The Mesozoic intrusions can be clearly pinpointed to the Late Jurassic and middle Early Cretaceous, and these intrusions are associated with gold mineralization in close spatial and temporal relationships and are

widely exposed in the Jiaobei uplift [34,43–45]. The Late Jurassic Linglong granitoids, emplaced in 165–150 Ma, host most of the gold deposits [46,47] and comprise biotite granite, quartz-diorite, and granodiorite. The middle Early Cretaceous Guojialing granitoids intruded the Linglong granitoids (Figures 1 and 2) [43,46] and consist of porphyritic quartz monzonite, granodiorite, and monzogranite, with large K-feldspar megacrysts. These granitoids contain Neoproterozoic, Paleoproterozoic, and Neoproterozoic xenocrystic zircons [34,43,44,47].

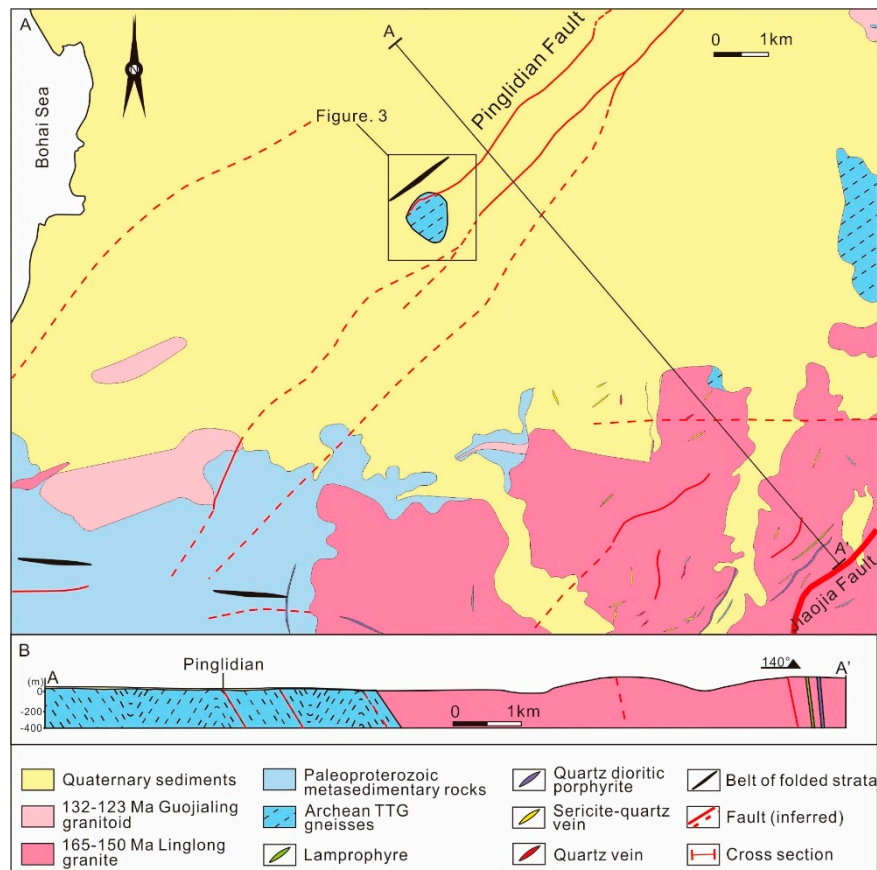


Figure 2. Sketch geological map of the northwestern Jiaodong gold province. (A) The Pinglidian gold deposit is situated within the Archean Jiaodong Group’s metamorphic rocks in the hanging wall of Jiaojia Fault. (B) Inferred cross section of AA’ in (A) to reveal the regional structure pattern (modified from unpublished internal material owned by Sanshandao Gold Company).

EW- to ENE-trending regional folding is well developed in the Precambrian metamorphic basement, such as Qixia anticlinorium and Laiyang anticlinoria [28,30]. NNE- to NE-trending fault systems rigidly controlled most of the gold mineralization that is hosted in the Mesozoic granitoids in the Jiaobei uplift [9,26]. From west to east, these fault systems are the Sanshandao Fault, Jiaojia Fault, and Zhaoping Fault, which are considered to be second-order faults of the lithospheric-scale Tan-Lu Fault [48–50]. These NNE- to NE-trending fault systems mainly follow the contact boundary between Mesozoic granitoid rocks in the footwall and Precambrian metamorphic rocks in the hanging wall, and partially cut through the Mesozoic granitoids and Precambrian metamorphic rocks. The lithological contacts along these faults, alongside fault jogs, exhibited the most control on the occurrence and distribution of the gold deposits (Figures 1 and 2). The gold deposits preferentially occurred in these jogs because of heterogeneous strain and increased fracture permeability, which focused ore fluid flow into their areas of influence [51–53], and fluid thus reacted with the wall rock. Second-order N- to NNE-trending faults, such as the Wang’ershan Fault in the footwall and Pinglidian Fault in the

hanging wall, overprinted the Qixia anticlinorium in the Precambrian metamorphic basement [30], are broadly parallel to the Jiaojia Fault, and converge with the Jiaojia Fault at depth [13] (Figure 2).

3. Geology of the Pinglidian Gold Deposit

3.1. Ore Geology

The Pinglidian gold deposit is located approximately 13 km to the northeast of Laizhou City in Pinglidian, Shandong Province. The Pinglidian gold deposit, occupying an area of 1.2 km², is one of the few auriferous quartz-vein gold deposits that are hosted in Archean metamorphic rock instead of Mesozoic granite in the northwestern area of the Jiaobei uplift, with a proven reserve of >5 t of gold (Figure 3). This deposit has been exploited since 1996 by the 10th team of the Chinese Army, with the gold grade varying from 1.7 to 47.02 g/t.

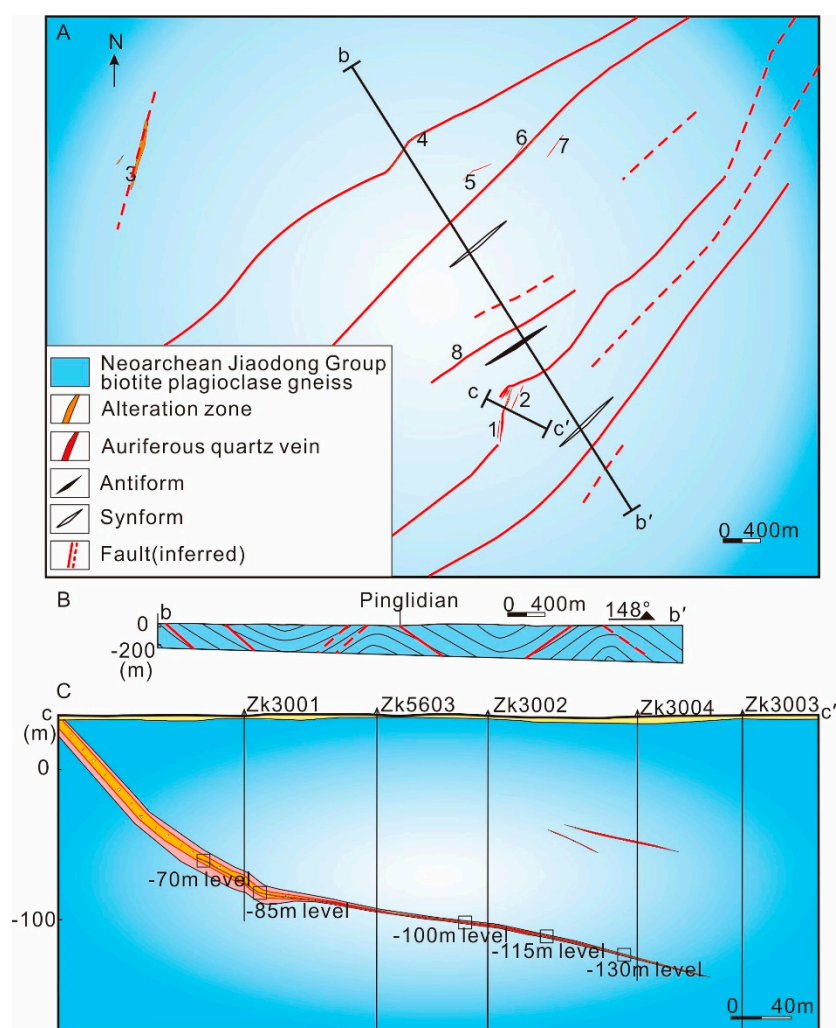


Figure 3. Simplified geological map and sketch map of the hydrothermal alteration zone and orebody in the Pinglidian gold deposit, showing the Archean basement fault's structural control on mineralization and hydrothermal alteration. (A) Plan view of an outcrop of the Pinglidian gold deposit. (B) Idealized regional scale ore-controlling structures of section bb' in Figure 3A. (C) The No. 1 orebodies controlled by local scale fault of section bb' in Figure 3A (modified from unpublished internal material owned by Sanshandao Gold Company).

Outcrops are rare in the ore district, covered by Paleogene sedimentary that is 1 m to 20 m thick. The host rock of the Pinglidian gold deposit is the Archean Jiaodong Group metamorphic

rock (Figure 4), which comprises biotite plagiogneiss and amphibolite gneiss (Figure 4A,B). The biotite plagiogneiss is gray to dark-gray in color and medium- to fine-grained lepidoblastic texture. The major minerals are plagioclase (55–70%), biotite (15–25%), and quartz (10–15%), and accessory minerals include magnetite, apatite, and zircon. The plagioclase amphibolite is grayish in color and shows medium- to fine-grained crystalloblastic textures (Figure 4C). The major minerals are plagioclase (45–60%), amphibole (30–40%), and biotite (10–15%), and accessory minerals include magnetite, apatite, and zircon (Figure 4D,E,F).

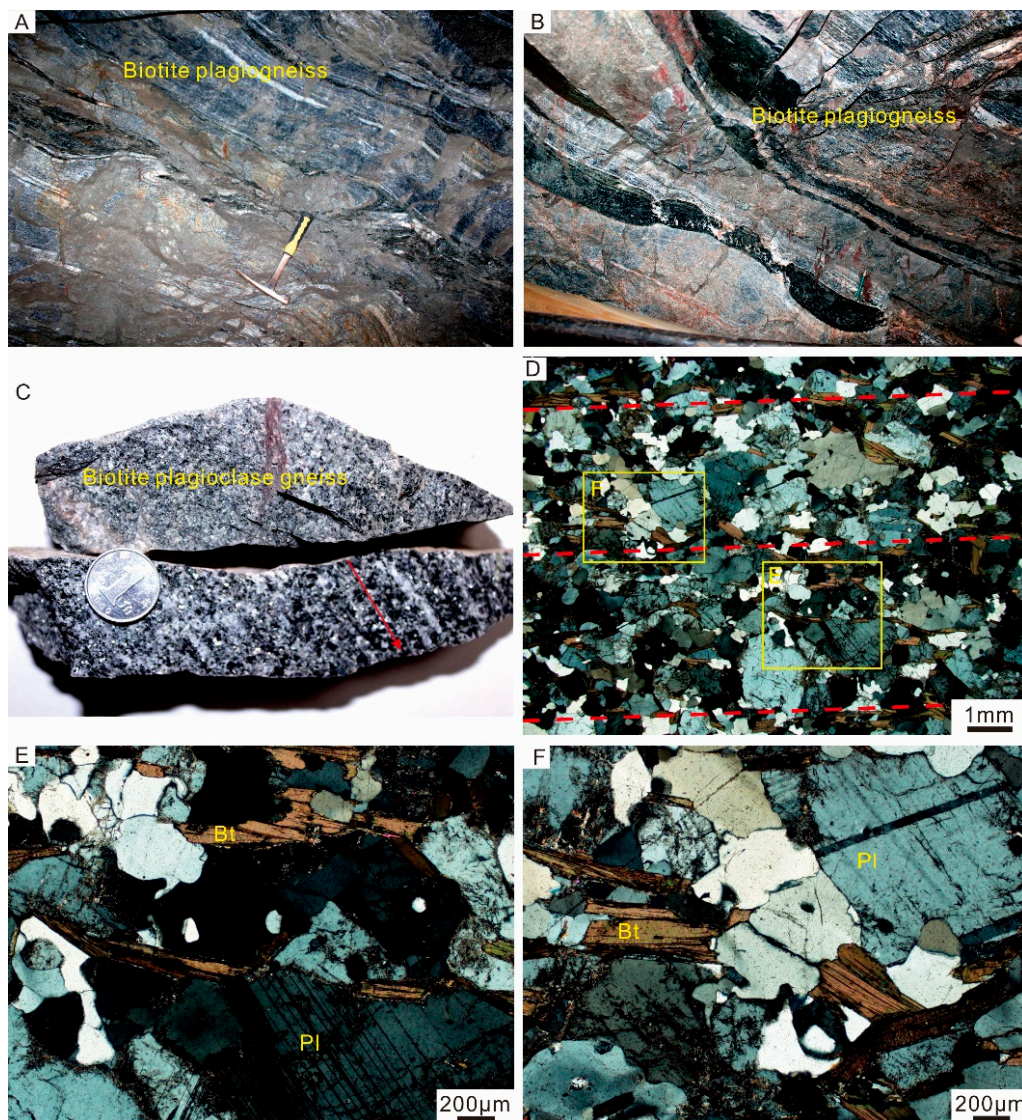


Figure 4. Field photographs (A,B), hand specimen (C), and transmitted-light photomicrographs (D–F) of mineral assemblages in biotite plagiogneiss. (A,B) The biotite plagiogneiss also experienced processes such as regional metamorphism and migmatization, resulting in schistosity and boudinage. (C) The main mineral assemblages of the biotite plagiogneiss is plagioclase and biotite, and accessory minerals include magnetite, apatite, and zircon. (D) Subhedral to anhedral plagioclase and biotite form the preferred orientation distribution in the protolith. (E,F) The deformation of biotite and plagioclase is apparent, with local recrystallization along the margins of the plagioclase.

Auriferous quartz veins are predominantly enveloped by a hydrothermal alteration halo in cataclastic zones, structurally controlled by the NE-trending and SE-dipping Pingliidian Fault and subsidiary faults. The Pingliidian Fault, generally striking 50° and dipping 30° SE, is approximately

15 km in length and 5–20 m in width. These faults controlled the occurrence of the No. 1 to No. 8 orebodies, which are tabular or lenticular in shape. The Pinglidian Fault is filled with cataclastic and brecciated rocks and fault gouges, which are a few centimeters to tens of centimeters thick. Locally, the occurrence of the Pinglidian Fault has rapidly varied to accommodate the wavy foliation in the metamorphic wall rock. The auriferous quartz veins predominantly occur along these faults and are parallel to the foliation in the wall rock, indicating that the fault was deformed and overprinted the Archean metamorphic rock.

3.2. Characteristic of the Orebodies

Eight auriferous quartz vein orebodies are present in the Pinglidian gold deposit (Figure 3). The No. 1 and No. 2 orebodies comprise more than 80% of the proven reserves in the Pinglidian gold deposit and are believed to be controlled by secondary faults in the hanging wall of the Jiaojia Fault (Figures 2 and 3), as described below.

The No. 1 orebody is the largest orebody in the Pinglidian gold deposit and is characterized by massive auriferous quartz vein ores in hydrothermal breccias and cataclastic rocks, including 1.8-m- to 18-m-thick zones of reddish alteration and sericite and quartz, with both disseminated pyrite and pyrite-quartz stockworks. The major orebody is tabular in shape and approximately 550 m long, with a strike of 15–42° and dip of 5–25° SE. The orebody extends gently dips down for up to 250 m, limited between the –70 m and –130 m levels and ranging from 0.2 m to 1.2 m (average of 0.62 m) in thickness. The gold grade varies from 1.7 to 47.02 g/t, with an average of 6.03 g/t.

The No. 2 orebody is much smaller than the No. 1 orebody and also exhibits massive auriferous quartz veins. This orebody generally strikes 33° and dips 7–10° SE, with a length of approximately 130 m. The No. 2 orebody gently dips down from the –28 m to –45 m levels, ranging from 0.4 m to 0.6 m (average of 0.36 m) in thickness. The gold grade varies from 12.8 to 24.7 g/t, with an average of 21.51 g/t.

3.3. Wall-Rock Alteration and Gold Mineralization

Gold mineralization that is associated with intense wall-rock alteration is controlled by the fault zone in Jiaodong. Auriferous quartz-vein orebodies, enveloped by hydrothermal alteration halos that are up to 18 m in width, symmetrically occur along the Pinglidian Fault. The spatial zonation of the four major types of mineral assemblages reveal the alteration zone from protolith (biotite plagiogneiss) to orebody (auriferous quartz vein) in the Pinglidian gold deposit. The wall-rock alteration includes sericitization, silicification, and pyritization. All these alterations are related to quartz veins that occur in two main alteration halos (reddish alteration zones and sericite-quartz alteration zones) between the protolith rock and auriferous quartz veins (Figure 5).

3.3.1. Protolith Rock and Reddish Alteration

The fresh protolith rock originated from Archean biotite plagiogneiss (Figure 4A), which has experienced the regional metamorphism of amphibolite facies under medium-pressure deformation. According to field observations, the biotite plagiogneiss also experienced regional metamorphism to migmatization, as evidenced by the formation of schistosity and boudinage (Figure 4A,B). These schistositities strike 50–53° and dip 15–42° SE in Pinglidian. Mineral lineation and foliation are well developed in the biotite plagiogneiss, according to hand species and thin sections (Figure 4C,D). The biotites are euhedral to subhedral plate crystals and are distributed with preferential orientation (Figure 4D,F). The plagioclase is subhedral to anhedral tabular crystals and usually occurs as polysynthetic twins (Figure 4D–F). Accessory minerals include magnetite, zircon, monazite, apatite, and titanite.

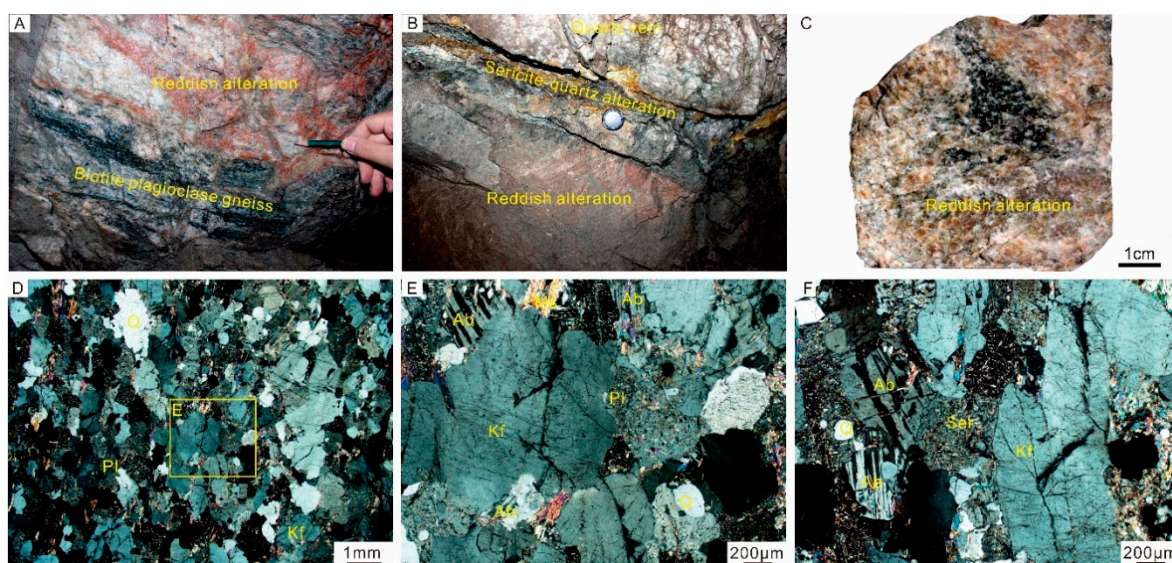


Figure 5. Field photographs (A,B), hand specimen (C), and transmitted-light photomicrographs (D–F) of mineral assemblages that are related to reddish alteration. (A) Biotite plagiogneiss was replaced by iron stained alteration, displaying a pinkish color. (B) Reddish alteration occurred in the outermost alteration halo, changing the quartz-vein orebody to biotite plagioclase gneiss. (C) The main mineral assemblages of the altered K-feldspar rock are secondary K-feldspar, albite, and quartz, with minor amounts of muscovite and relict plagioclase. (D) Relict plagioclase is surrounded by quartz, muscovite, and secondary K-feldspar. Albite is present in the altered rock. (E,F) In the heavily altered area, K-feldspar and muscovite completely replaced plagioclase, while some remnant plagioclase is very dirty with massive sericite. Brittle fractures cut through the secondary K-feldspar, some of which were filled with sericite.

Reddish alteration in the outermost area of the alteration veins (Figures 3E,I and 5A,B) envelops the gold mineralization, which is related to earlier quartz veins and is characterized by scarce K-feldspar and albite that transformed from plagioclase or biotite in Archean metamorphic rock (Figure 5C–F). The thickness of this reddish alteration zone varies from tens of centimeters to meters because of diffusion and the intensity of fluid-rock reactions. The main mineral assemblages of this reddish alteration rock include secondary K-feldspar, albite, and quartz, with minor amounts of K-feldspar, muscovite, and relict plagioclase (Figure 5C). Biotite is completely absent, and relict plagioclase is surrounded by subhedral or anhedral quartz, muscovite, and secondary K-feldspar and albite in the altered rock (Figure 5D). In some local areas, plagioclase was almost completely replaced by albite and muscovite, while some remnant plagioclase is turbid with massive sericite (Figure 5E,F). Brittle fractures cut through the new secondary K-feldspar, some of which were filled with sericite. Accessory minerals in the biotite plagiogneiss, such as pyrite, magnetite, apatite, and zircon, were also replaced by albite and quartz in the weak alteration zone. Preferentially oriented foliation and lineation are present in the protolith instead of massive structures.

3.3.2. Sericite-Quartz Alteration

Adjacent to the auriferous quartz veins, relatively narrow sericite-quartz alteration zones vary from tens of centimeters to meters in thickness and are associated with broad or narrowing quartz veins. A sericite-quartz alteration zone closely envelops the quartz-vein orebody, pinched within the broad cataclastic sericite-quartz alteration zone (Figure 6A). Intensive sericitization, silicification, and pyritization overprinted previous reddish alteration along brittle cracks or open spaces in the cataclastic zone. Dense sericite-quartz alteration partially filled in brittle fractures in the quartz veins and enclosed earlier quartz-vein breccia (Figure 6B). The sericite-quartz alteration that is adjacent to earlier quartz vein consists of dense sericite, quartz, and minor pyrite (Figure 6C). The quartz and

muscovite are distributed with preferential orientation in the dense sericite-quartz alteration zone (Figure 6D). Subhedral and anhedral quartz and muscovite are surrounded by a sericite matrix, and porphyroclasts show irregular shapes and various sizes (Figure 6E,F). Quartz is irregularly distributed in the sericite matrix in the sericite-quartz alteration zone (Figure 6G). Euhedral pyrite occurs in the sericite-quartz alteration zone, and anhedral galena filled in brittle fractures in pyrite (Figure 6H,I). A small amount of pyrite is disseminated within the sericite-quartz alteration rock. In addition, minor galena, which typically filled in cracks in pyrite, precipitated contemporaneously with the disseminated pyrite.

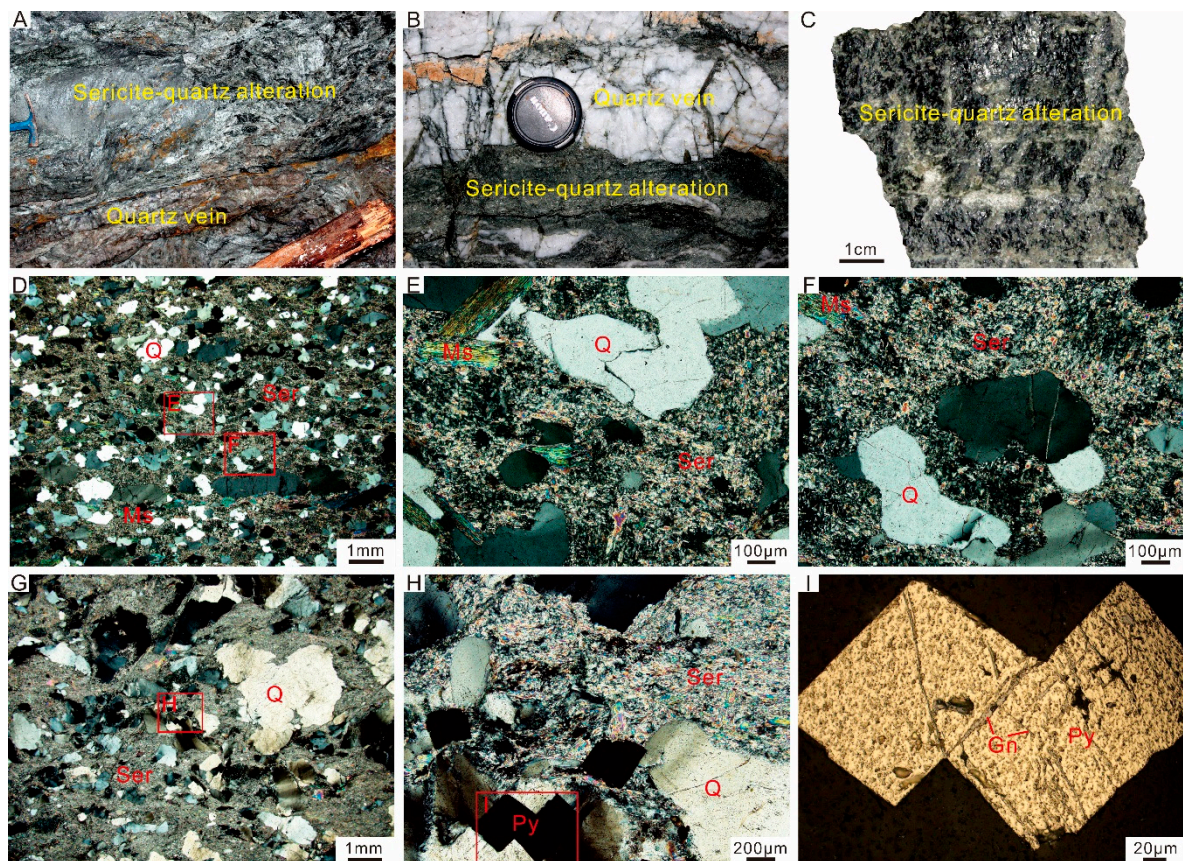


Figure 6. Field photographs (A,B), hand specimen (C), transmitted-light photomicrographs (D–H), and reflected-light photomicrographs of mineral assemblages that are associated with the sericite-quartz alteration zone. (A) The sericite-quartz alteration zone closely envelops the quartz vein orebody, which is pinched within the broad cataclastic sericite-quartz alteration zone. (B) Dense sericite-quartz alteration partially filled in brittle fractures in quartz veins and encloses the earlier quartz-vein breccia. (C) The sericite-quartz alteration that is adjacent to earlier quartz veins consists of dense sericite, quartz, and minor pyrite. (D) Quartz and muscovite are distributed along preferred orientations in the dense sericite-quartz alteration zone. (E,F) Subhedral and anhedral quartz and muscovite are surrounded by a sericite matrix, and porphyroclasts show irregular shapes and various sizes. (G) Quartz is irregularly distributed in the sericite matrix in the sericite-quartz alteration zone. (H,I) Euhedral pyrite occurred in the sericite-quartz alteration zone, and anhedral galena filled in brittle fractures in pyrite.

3.3.3. Quartz Veins and Gold Mineralization

Quartz veins occur in the center of the hydrothermal alteration halo. Two types of quartz veins could be identified from the cutting relationships and mineral assemblages. Type-I early quartz veins are milky in color and relatively broad and mainly consist of quartz (>90%) and minor muscovite and plagioclase (Figure 7A). These type-I quartz veins contain almost no gold, even if small pyrite veins or phenocrysts are present. Cataclastic texture is well developed in these early type-I quartz veins.

Younger brittle fractures overprinted the older broad quartz veins (Figure 7B). Type-II late quartz veins are gray to dark gray in color, have varying thickness, and commonly cut through the type-I quartz veins (Figure 7C). The type-II quartz veins predominantly consist of quartz (>80%), galena, and pyrite, with minor chalcopyrite and sphalerite (Figure 7D), and are closely associated with gold mineralization in the Pingliadian gold deposit. These type-II quartz veins have partially or completely replaced any type-I quartz veins.

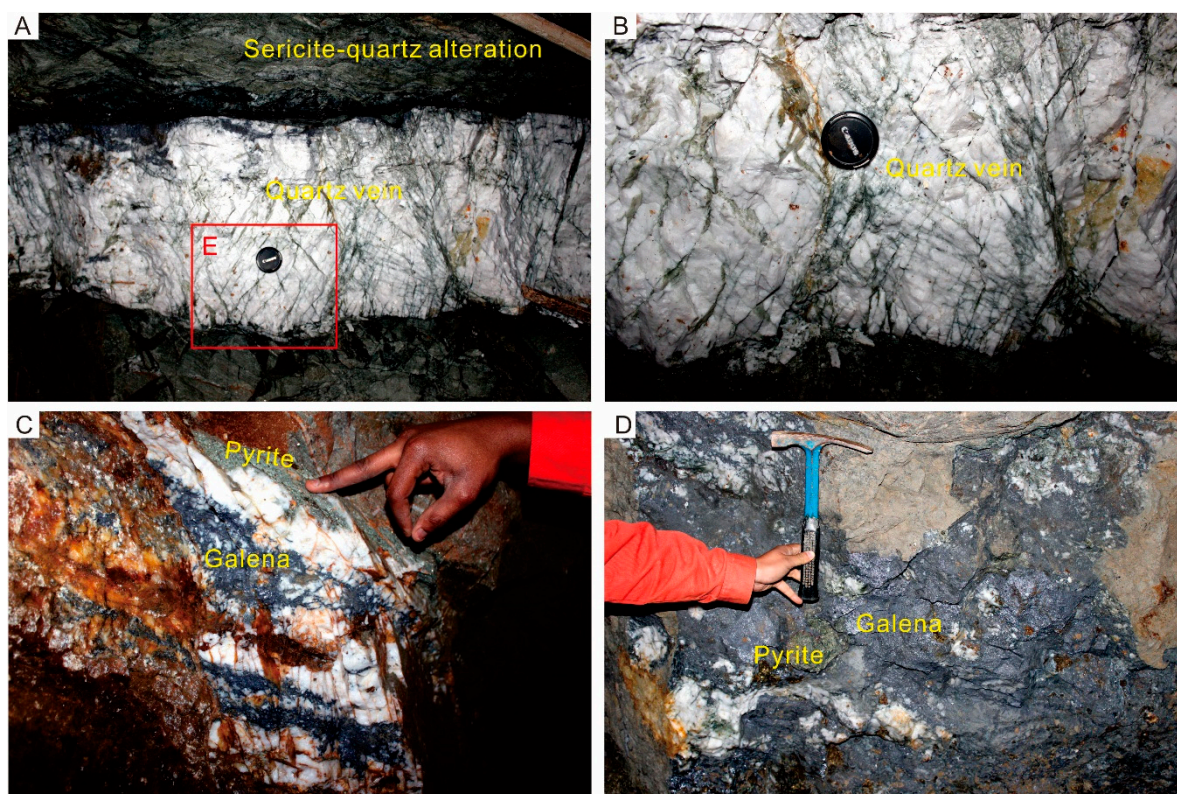


Figure 7. Field photographs that show two types of quartz veins in the Pingliadian gold deposit. (A) This type-I broad milky quartz vein that contains almost no gold, with a few tiny pyrite veins or phenocrysts. (B) Late brittle fractures overprinted the early broad quartz vein. (C) This type-II quartz sulfide vein cut through the type-I quartz vein. (D) The type-II quartz sulfide vein predominantly consists of quartz, galena, pyrite, chalcopyrite, and sphalerite, which have partially or completely replaced the type-I quartz vein ore.

Based on the mineral assemblages and distributions, the ores could be divided into disseminated- (Figure 8A) and massive sulfide ores (Figure 8B,C). The former comprises sericite-quartz or milky quartz veins with disseminated or veinlet mineral assemblages in the center of alteration halos and represents early gold mineralization (stage I), associated with cataclases and breccias. The quartz-pyrite veinlets (stage II) and massive quartz-sulfide (stage III) ores (Figure 8B,C) represent the main period of gold mineralization, and are associated with changing physicochemical conditions during ore formation in the hydrothermal alteration zones. Anhedral pyrite (stage II) experienced brittle deformation, with some fracture networks filled with younger material (Figure 8D). Some intergranular gold and galena filled in brittle fractures in the stage II pyrite (Figure 8E). The stage-III massive sulfide ore is associated with complex assemblages, including pyrite, galena, pyrrhotite, chalcopyrite, sphalerite, freibergite, and tetrahedrite (Figure 8F–I). Anhedral pyrite was replaced and enclosed by anhedral galena, which is the predominant mineral in the stage-III ores (Figure 8G). Euhedral pyrite coexists with pyrrhotite and galena (Figure 8H). Anhedral pyrite, chalcopyrite, and

sphalerite are commonly present in the stage-III ore (Figure 8I). Quartz-carbonate ore is rare, and used to be considered as stage-IV ore and filled in any brittle fractures.

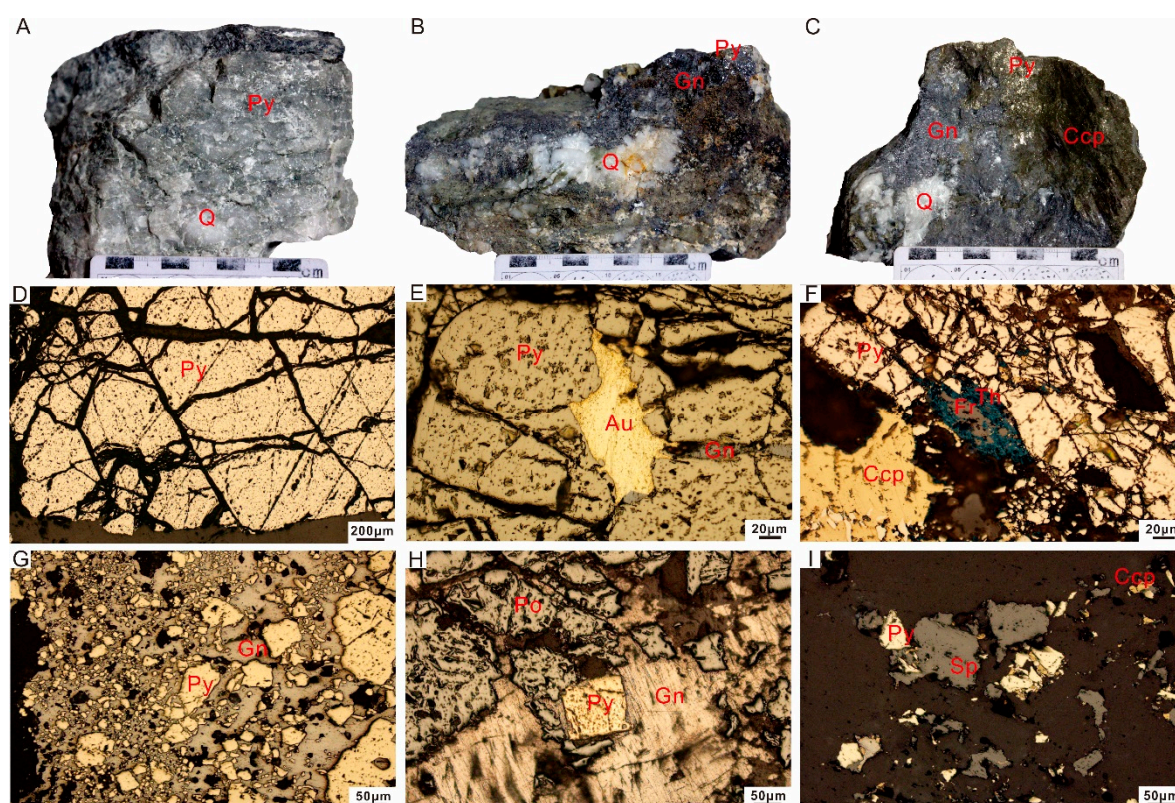


Figure 8. Ore and mineral assemblages in the Pinglidian gold deposit. (A) Quartz, pyrite, and sericite (Stage I). (B) Quartz, pyrite, galena, and chalcopyrite (Stages II and III). (C) Quartz and galena accumulations (Stage III). (D) Fracture network that was filled with anhedral pyrite (Stage III). (E) Intergranular gold and galena that were associated with brittle fractures in pyrite. (F) Pyrite, chalcopyrite, freibergite, and tetrahedrite. (G) Anhedral pyrite that was replaced and enclosed by anhedral galena. (H) Euhedral pyrite, pyrrhotite, and galena. (I) Anhedral pyrite, chalcopyrite, and sphalerite. Au, gold; Ccp, chalcopyrite; Fr, freibergite; Gn, galena; Py, pyrite; Po, pyrrhotite; Q, quartz; Ser, sericite; Sp, sphalerite.

Visible gold occurs as native gold and electrum; the latter comprises more than 90% of the observed visible gold. Visible gold is generally intergrown with anhedral pyrite and galena, and sometimes occurs in brittle fractures in the subhedral to anhedral pyrite or the matrix of the quartz veins (Figure 9A). Meanwhile, brittle cataclastic textures of pyrite are commonly filled with galena (Figure 9A). Electrum is elongated along anhedral galena-deformation fabrics (Figure 9A,B), and native gold shows exsolution texture within the electrum (Figure 9B). Visible gold mainly occurs as irregularly shaped electrum in pyrite and galena in the quartz veins (Figure 9C,D).

3.3.4. Paragenetic Sequences

Four paragenetic sequences have been identified based on the presence of alteration halos (Figure 10), cross-cutting relationships of the mineralized quartz veins or sulfide veinlets, and mineralogical and textural characteristics of the ores to interpret the gold mineralization of the Pinglidian gold deposit (Figures 4–9). As mentioned above, these sequences include quartz-sericite alteration (stage I), quartz-pyrite veinlets (stage II), massive quartz-sulfide veins (stage III), and carbonate (stage IV). The detailed paragenetic sequence of the Pinglidian gold deposit is summarized in Figure 10. Biotite, plagioclase, K-feldspar, and albite occurred before gold mineralization. Pyrite and

quartz are the principal visible gold-hosting minerals throughout the entire gold mineralization, from stage I to IV. Native gold and electrum are rare in stages I and IV but are developed in stages II and III. In terms of sulfides, stage III consists of galena, followed by pyrite, chalcopyrite, sphalerite, pyrrhotite, freibergite, and tetrahedrite. In addition, sericite predominantly occurs in stage I, and calcite normally appears in late stage IV material.

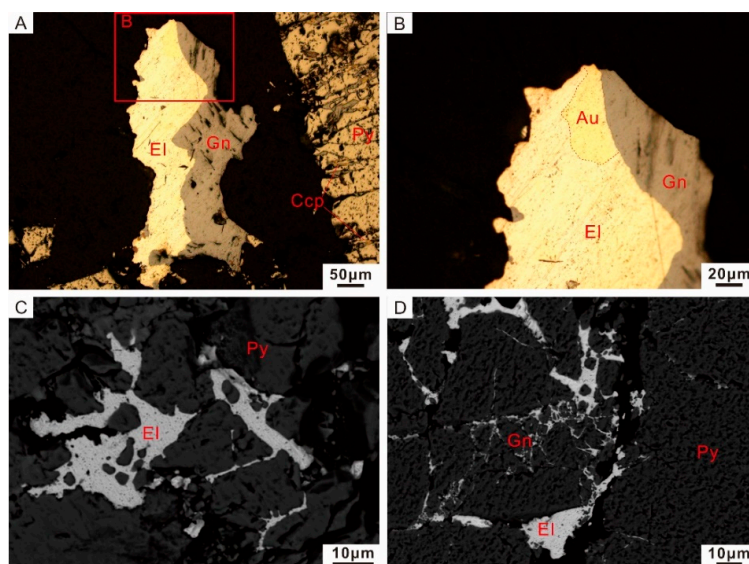


Figure 9. Reflected-light photomicrographs (A,B) and back-scattered electron (BSE) images (C,D) of gold in the ore. (A) Electrum intergrowth with galena. (B) Native gold that coexists with electrum. (C,D) Pyrite, galena, and electrum in a quartz vein.

Mineral	Stage I	Stage II	Stage III	Stage IV
Quartz	—	—	—	—
Sericite	—	—	—	—
Pyrite	—	—	—	—
Pyrrhotite	—	—	—	—
Native gold	—	—	—	—
Electrum	—	—	—	—
Galena	—	—	—	—
Chalcopyrite	—	—	—	—
Sphalerite	—	—	—	—
Tetrahedrite	—	—	—	—
Freibergite	—	—	—	—
Calcite	—	—	—	—

Figure 10. Paragenetic sequence of the Pingliidian gold deposit as interpreted from the field-cutting relationships, ore textures, and mineral assemblages that were associated with gold mineralization. The line thickness shows the relative abundance of minerals in the paragenetic sequence, as summarized from the above evidence.

4. Analysis Methods and Results

4.1. Electron Probe Microanalyses (EPMA)

Five samples (7 analyses on electrum, 4 analyses on pyrite, 4 analyses on galena, and 3 analyses on chalcopyrite) were analyzed. Quantitative chemical analyses of these 5 samples were conducted by using a JXA-8230 electron microprobe with an accelerating voltage of 15 kV and beam current of 20 nA at the Institute of Mineral Resources, Chinese Academy of Geological Sciences (CAGS), Beijing. Natural minerals and synthetic oxides were used as standards.

The EPMA results are shown in Table 1. Seven spot analyses of visible gold showed electrum contents (in wt %) of 55.92–72.15 for Au, 25.8–43.67 for Ag, 0.14–0.67 for Bi, and 0.03–0.07 for Te. Four spot analyses of pyrite showed elemental contents (in wt %) of 53.42–53.67 for S, 45.8–43.67 for Fe, 0.11–0.21 for Pb, and 0.04–0.06 for Au. Four spot analyses of galena showed elemental contents (in wt %) of 13.34–13.74 for S, 86.28–86.39 for Pb, 0.07–0.15 for Cd, and 0.21–0.3 for Bi. Three spot analyses of chalcopyrite showed elemental contents (in wt %) of 33.94–34.58 for S, 30.24–32.22 for Fe, 31.61–33.72 for Cu, 0.09–0.2 for Pb, 0.06–0.11 for Zn, and 0.11–0.15 for Bi.

Table 1. Representative electron probe microanalyses of metallic minerals from the Pingliidian gold deposit.

Samples	Au	Ag	S	As	Se	Fe	Zn	Pb	Cu	Sb	Cd	Bi	Te	Total (%)	Mineral
02B1-1	71.37	28.30	0.04	/	/	/	/	/	/	/	0.06	0.15	/	99.92	Electrum
02B1-2	62.19	36.89	0.05	/	/	/	/	/	/	/	0.07	0.67	0.05	99.92	Electrum
02B1-3	59.03	39.64	0.11	/	/	0.63	/	/	/	/	/	0.48	0.03	99.92	Electrum
02B1-4	72.86	25.80	0.03	/	/	0.62	/	/	/	/	/	0.61	/	99.92	Electrum
02B1-5	71.65	27.51	0.02	0.06	/	0.42	/	/	/	0.05	/	0.23	0.04	99.98	Electrum
02B1-6	55.92	43.67	/	/	0.06	0.14	/	/	/	/	/	0.14	0.05	99.98	Electrum
02B1-7	72.15	26.86	/	/	/	0.19	/	/	/	/	/	0.57	0.07	99.84	Electrum
14B2-1	/	/	34.42	/	/	30.44	0.06	0.14	34.23	/	/	/	/	99.29	Chalcopyrite
20B1-2	/	/	34.58	0.07	/	30.24	/	0.09	33.72	/	/	0.15	0.03	98.88	Chalcopyrite
28B1-2	0.08	0.72	33.94	/	/	32.22	0.11	0.20	31.61	/	0.06	0.11	/	99.05	Chalcopyrite
16B1-1	/	/	13.46	/	/	/	/	86.3	/	/	0.07	0.29	0.07	100.19	Galena
16B1-2	/	/	13.74	/	/	0.06	/	86.28	/	/	0.15	0.21	0.03	100.47	Galena
20B1-1	/	/	13.34	/	/	/	/	86.39	/	0.04	0.11	0.30	/	100.18	Galena
28B1-1	/	/	13.55	/	/	0.12	/	85.34	/	/	0.10	0.29	/	99.40	Galena
14B2-2	/	/	53.67	0.04	/	46.22	/	0.14	/	/	/	0.11	/	100.18	Pyrite
16B1-3	0.04	/	53.52	/	/	46.40	/	0.11	/	/	/	/	0.03	100.10	Pyrite
20B1-3	/	0.09	53.42	/	/	46.05	/	0.16	0.11	/	0.03	/	/	99.86	Pyrite
28B1-3	0.06	/	53.57	0.05	0.03	45.80	/	0.21	/	/	0.04	/	/	99.76	Pyrite

Note: “/” means the abundance is below the determination limits, 320 ppm for Au, 173 ppm for Ag, 99 ppm for S, 250 ppm for As, 227 ppm for Se, 199 ppm for Fe, 197 ppm for Zn, 421 ppm for Pb, 169 ppm for Cu, 350 ppm for Sb, 266 ppm for Cd, 460 ppm for Bi, and 297 ppm for Te.

4.2. Bulk Geochemistry

4.2.1. Major and Trace Elements

Thirteen samples (3 for biotite plagiogneiss, 4 for reddish alteration, and 6 for sericite-pyrite alteration) were collected to analyze the whole-rock major- and trace-element concentrations. Quantitative analysis was performed by using a Philips PW2404 X-ray Fluorescence Spectrometer (XRF) and an ELEMENT-1 plasma mass spectrometer (Finnigan-MAT Ltd.) at the Research Institute of Uranium Geology, Beijing, China. The analytical uncertainties were less than $\pm 1\%$ and $\pm 5\%$ for major and trace elements, respectively. The detailed analytical procedures are described in Li et al. [54].

4.2.2. Geochemical Characteristics of the Original and Altered Rock

Thirteen samples were classified into two groups according to their major-element concentrations, except for two abnormal samples (e.g., 17B1 is short for PLD15D017B1, and 24B2 is short for PLD15D024B2), as listed in Table 2 and Figure 11. The concentrations of SiO_2 (67.62–75.77%) and Al_2O_3 (12.8–18.8%) remained high and relatively stable (Table 2; Figure 11E). K_2O (1.02–5.94%) and LOI (1.01–4.37%) exhibited increasing concentrations from biotite plagiogneiss and albitized rock to sericite-quartz altered rock (Figure 11A,F), while Na_2O (0.213–5.49%) and CaO (0.154–3.02%) showed decreasing concentrations (Figure 11B,C). Fe_2O_3 (0.65–5.23%) showed a negative correlation with SiO_2 (Figure 11D).

The original and altered rock also exhibited variable chondrite-normalized rare-earth-element (REE) patterns and primitive mantle-normalized trace-element patterns [55] (Figure 12), including LILEs, HFSEs, and TRTEs. The whole-rock REE and trace-element patterns could be classified into four groups in accordance with biotite plagiogneiss, reddish alteration, sericite-quartz alteration, and quartz veins (Tables 2 and 3, Figures 12 and 13).

Table 2. Major oxides (wt %) and trace elements (ppm) for wall-rock samples from the Pingliadian gold deposit.

Samples	Biotite Plagioclase Gneiss			Reddish Altered Rock				Sericite-Quartz Altered Rock					
	07B3	13B1	18B5	04B1	17B1	18B4	27B1	02B2	03B2	07B2	14B1	19B2	24B2
SiO ₂	70.96	67.62	74.34	75.77	58.24	72.84	72.09	72.47	75.02	67.57	68.18	69.16	58.67
Al ₂ O ₃	15.24	16.11	14.34	13.64	16.46	13.82	13.55	12.80	15.30	15.42	18.80	14.49	19.60
Fe ₂ O ₃	2.22	2.78	0.76	0.65	7.91	3.19	1.80	5.23	1.66	4.14	2.32	2.98	3.05
MgO	1.30	1.92	0.43	0.28	3.22	0.78	0.73	2.23	0.56	2.14	0.79	0.85	1.14
CaO	2.31	3.02	2.61	1.26	6.57	1.45	2.53	0.38	0.15	0.98	0.41	2.85	1.33
Na ₂ O	5.08	4.86	5.27	5.49	4.64	5.07	4.5	0.25	0.21	3.76	0.28	0.34	0.18
K ₂ O	1.35	1.54	1.02	1.29	0.84	1.29	1.65	3.30	4.57	2.55	5.94	4.40	6.11
MnO	0.03	0.04	0.02	0.03	0.21	0.04	0.04	0.08	0.02	0.03	0.01	0.09	0.08
TiO ₂	0.27	0.39	0.06	0.06	0.80	0.21	0.19	0.25	0.12	0.44	0.12	0.29	0.20
P ₂ O ₅	0.09	0.11	0.03	0.03	0.14	0.06	0.06	0.12	0.04	0.15	0.03	0.09	0.05
LOI*	1.04	1.48	1.01	1.49	0.86	1.12	2.81	2.81	2.24	2.75	3.02	4.37	4.55
TOTAL	99.91	99.89	99.90	100.00	99.90	99.89	99.96	99.94	99.91	99.94	99.93	99.93	94.99
B	9.42	10.50	10.80	10.90	7.69	8.59	10.30	27.20	34.60	11.40	32.50	14.20	24.10
Li	20.40	25.40	5.31	4.73	20.60	19.50	6.11	15.50	3.51	16.30	3.15	11.40	4.30
Be	0.84	1.27	0.99	0.63	1.21	0.97	0.61	1.30	1.45	0.86	1.69	1.14	1.61
Sc	3.96	5.09	1.35	1.29	16.80	3.35	2.70	3.43	1.63	5.18	2.03	4.23	2.67
V	28.00	46.60	10.50	10.80	127.00	28.10	14.30	28.80	12.80	41.80	30.30	25.90	28.50
Cr	5.03	8.19	2.72	3.03	23.10	7.46	2.96	4.86	2.98	8.87	2.25	4.93	2.24
Co	5.50	8.83	1.06	0.97	16.20	3.16	3.27	5.87	2.13	8.08	3.08	3.51	2.28
Ni	3.98	12.80	1.39	1.56	24.30	3.50	1.84	5.19	1.62	6.44	3.82	3.34	2.53
Cu	4.01	25.60	5.51	44.20	35.90	6.74	14.90	12.60	112.00	5.34	9.95	18.80	49.10
Zn	49.60	54.10	19.20	18.80	142.00	81.00	33.80	316.00	43.20	70.50	36.80	59.00	56.50
Ga	19.10	18.20	17.20	14.60	22.80	19.60	15.80	17.60	18.90	20.60	23.20	18.00	24.40
Rb	45.40	53.30	19.60	39.90	14.00	34.10	49.40	97.60	129.00	98.10	154.00	130.00	174.00
Sr	286	382	248	226	303	209	138	25.20	9.97	84.70	10.70	46.40	40.20
Y	5.49	5.60	3.09	2.23	19.80	6.91	4.32	6.78	5.24	8.44	1.52	6.69	3.93
Mo	0.14	0.13	0.14	0.11	0.49	0.15	0.18	0.20	0.15	0.21	1.09	0.13	0.05
Cd	0.15	0.13	0.16	0.15	0.44	0.34	0.14	4.16	0.44	0.25	0.29	0.16	8.51
In	0.02	0.02	0.01	0.01	0.07	0.02	0.01	0.02	0.02	0.03	0.05	0.03	0.11
Sb	0.08	0.11	0.07	0.18	0.08	0.16	0.20	0.41	0.46	0.26	0.27	0.45	4.73
Cs	1.93	1.44	1.30	1.17	0.41	1.66	1.88	1.42	1.90	2.10	2.04	2.94	2.54
Ba	252	374	133	220	102	171	228	207	270	779	723	387	571
La	19.70	17.00	9.59	4.69	14.70	23.30	7.14	16.10	24.40	28.50	9.39	22.50	18.70
Ce	34.70	32.10	17.80	8.40	31.10	43.60	12.60	30.30	45.50	53.20	17.20	39.10	31.70
Pr	3.81	3.78	2.03	0.94	3.89	4.90	1.40	3.46	5.12	5.94	1.90	4.23	3.27
Nd	13.70	14.90	7.53	3.38	15.70	17.90	5.49	13.20	19.50	21.40	7.07	15.20	11.40
Sm	2.22	2.36	1.37	0.66	3.29	3.23	1.04	2.28	3.46	3.37	1.06	2.66	1.67
Eu	0.78	0.78	0.57	0.42	1.41	0.68	0.44	0.51	0.46	0.85	0.26	0.77	0.47
Gd	1.92	2.01	1.16	0.55	2.92	2.67	0.95	1.89	2.82	2.96	0.91	2.29	1.48
Tb	0.27	0.28	0.16	0.09	0.61	0.40	0.17	0.29	0.37	0.41	0.11	0.33	0.18
Dy	1.22	1.28	0.66	0.43	3.26	1.61	0.79	1.40	1.47	1.87	0.39	1.49	0.78
Ho	0.21	0.21	0.12	0.08	0.67	0.27	0.15	0.25	0.20	0.31	0.06	0.24	0.14
Er	0.59	0.58	0.32	0.22	1.90	0.72	0.43	0.69	0.50	0.90	0.16	0.64	0.42
Tm	0.09	0.08	0.04	0.04	0.33	0.10	0.07	0.11	0.06	0.13	0.02	0.09	0.07
Yb	0.45	0.48	0.29	0.23	2.05	0.60	0.41	0.63	0.38	0.77	0.11	0.55	0.41
Lu	0.07	0.06	0.04	0.03	0.31	0.09	0.06	0.10	0.05	0.12	0.02	0.07	0.06
W	0.47	0.16	1.78	2.36	1.01	5.58	1.51	3.02	8.80	2.22	7.67	3.49	8.36
Re	0.005	0.004	0.003	<0.002	0.008	0.006	0.006	<0.002	0.002	0.002	0.007	<0.002	0.002
Tl	0.22	0.24	0.08	0.19	0.08	0.14	0.24	0.53	0.68	0.45	0.75	0.63	0.88
Pb	9.44	242	108	30.30	261	61.40	71.90	337	2081	10.70	165	85.90	35622
Bi	0.03	0.43	0.16	0.05	0.45	0.17	0.04	0.06	0.07	0.05	0.30	0.02	2.61
Th	2.39	1.88	1.87	0.76	2.03	4.94	1.41	2.07	4.37	3.43	2.03	2.88	2.44
U	0.41	1.96	0.36	0.49	1.24	0.42	0.41	1.17	1.07	0.96	1.26	0.29	0.37
Nb	4.49	6.40	1.94	2.62	10.50	5.07	3.39	5.53	4.40	8.22	1.54	7.73	3.75
Ta	0.29	0.78	0.23	0.18	0.81	0.28	0.23	0.44	0.38	0.50	0.11	0.37	0.35
Zr	23.50	27.70	31.50	27.00	11.80	49.10	42.60	53.40	31.00	54.00	21.30	46.10	51.70
Hf	0.70	0.69	0.97	0.94	0.63	1.49	1.25	1.44	1.12	1.24	0.61	1.15	1.43
Eu/Eu*	1.14	1.08	1.34	2.08	1.36	0.69	1.33	0.74	0.44	0.81	0.81	0.93	0.90
Ce/Ce*	0.92	0.94	0.94	0.92	0.99	0.95	0.92	0.95	0.95	0.95	0.94	0.92	0.91
ΣREE	79.77	75.94	41.71	20.2	82.16	100.09	31.17	71.23	104.32	120.75	38.67	90.2	70.78
LREE/HREE	15.45	14.17	13.79	10.88	5.81	14.46	9.19	12.26	16.75	15.13	20.65	14.73	18.85
(La/Yb) _N	31.13	25.30	23.48	14.38	5.14	27.86	12.34	18.27	45.94	26.51	59.08	29.08	32.48
(Sm/Yb) _N	5.43	5.44	5.20	3.15	1.78	5.98	2.78	4.01	10.09	4.86	10.33	5.33	4.49
(La/Sm) _N	5.73	4.65	4.52	4.57	2.88	4.66	4.43	4.56	4.55	5.46	5.72	5.46	7.23

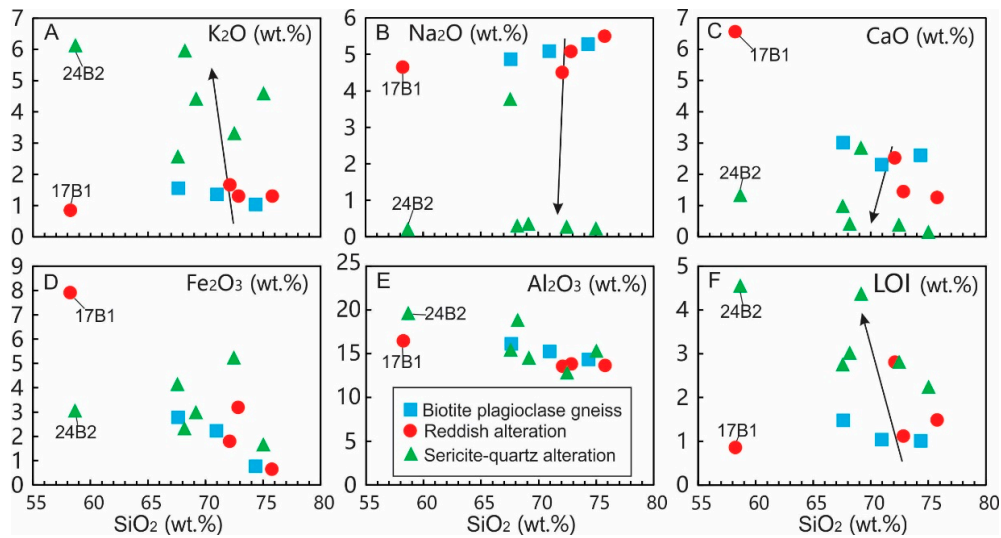


Figure 11. Selected plots of the wall rock in the Pingliadian gold deposit. Thirteen samples can be generally classified into two groups according to the major-element concentrations, except for two abnormal samples (17B1 and 24B2). (A,F) K₂O vs. SiO₂ and LOI vs. SiO₂ diagrams, which show increasing concentrations from the biotite plagioclase gneiss and albitized rock to sericite-quartz alteration rock. (B,C) Na₂O vs. SiO₂ and CaO vs. SiO₂ diagrams, which show decreasing concentrations. (D,E) Fe₂O₃ vs. SiO₂ and Al₂O₃ vs. SiO₂ diagrams, which show relatively stable concentrations.

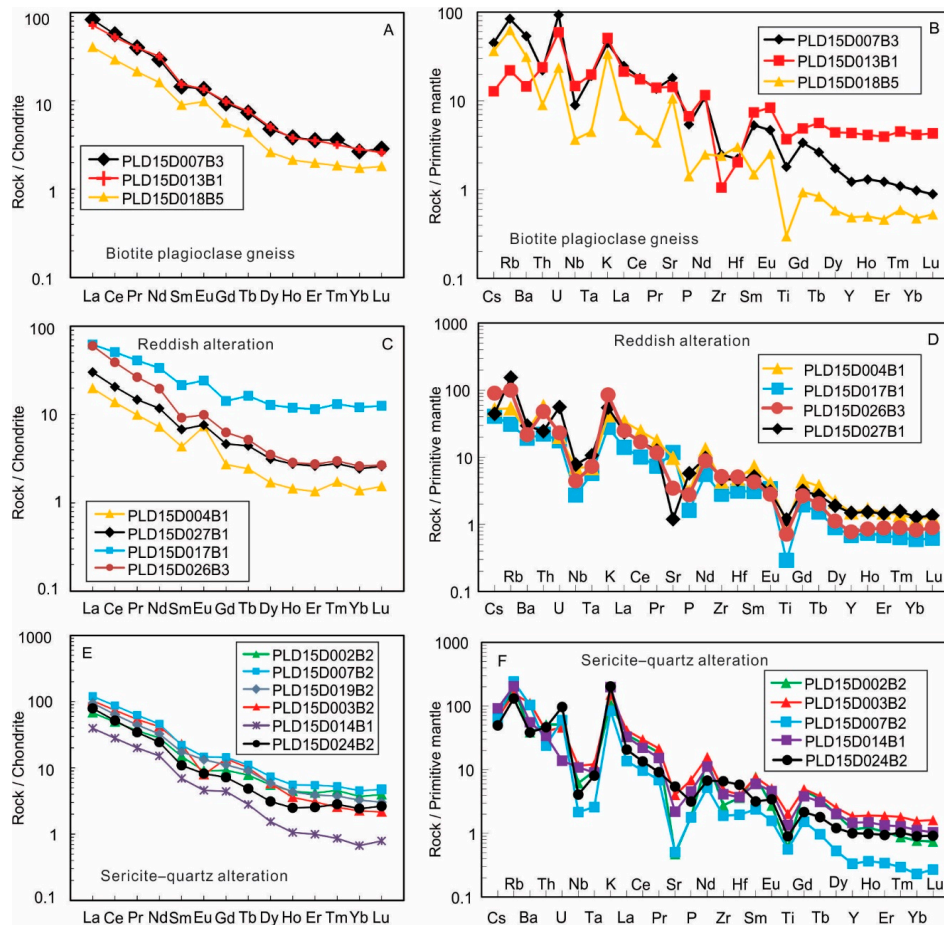


Figure 12. Chondrite-normalized REE patterns and primitive mantle-normalized trace-element patterns for biotite plagiogneiss, reddish alterations, and sericite-quartz alterations in the Pingliadian gold deposit. The chondrite- and primitive mantle-normalization data are from [55].

Table 3. Trace elements (ppm) for two types of quartz vein from the Pingliidian gold deposit.

Samples	Type I Quartz Veins						Type II Quartz Vein							
	14B3	18B1	19B1	20B2	23B2	02B1	03B1	08B1	11B1	14B2	23B1	26B1	26B2	27B3
Li	11.70	11.70	2.65	6.07	6.76	1.85	2.63	1.08	0.776	1.34	0.26	0.25	2.11	0.90
Be	0.87	0.07	0.08	0.04	0.04	0.08	0.17	0.01	0.01	0.12	0.01	0.04	0.05	0.002
Sc	8.66	0.96	0.39	0.15	0.62	2.04	0.39	0.35	0.73	3.72	0.80	0.31	0.57	0.15
V	70.60	2.97	0.58	0.97	3.58	4.32	5.18	5.93	0.83	5.76	0.04	2.41	0.33	1.07
Cr	7.22	3.14	7.05	1.73	10.80	2.17	3.89	2.01	1.61	1.39	1.36	1.70	2.93	1.88
Co	8.74	1.13	1.29	1.22	3.29	21.00	8.25	28.10	0.59	7.97	0.05	2.95	0.04	6.77
Ni	6.72	2.65	2.95	0.93	8.03	26.00	10.20	40.20	1.38	11.00	0.67	4.46	0.52	12.90
Cu	15.10	293	10.20	825	4780	57.50	2154	4356	4131	10647	1.67	321	1.35	28
Zn	70.40	445	18.90	124	12.50	87.80	5059	13.40	56.70	140	1.49	20.90	8.05	6.70
Ga	21.80	2.75	0.82	0.52	1.15	1.61	1.43	0.23	0.53	1.38	0.07	0.71	0.31	0.32
Rb	143	2.46	2.40	1.27	1.53	0.39	9.87	0.55	0.12	1.86	0.07	0.14	0.11	0.18
Sr	140	24.90	25.60	5.95	17.10	36.60	11.30	5.51	16.70	311	2.82	1.04	3.18	10.90
Y	9.85	3.21	2.05	0.56	0.27	4.07	1.40	0.49	2.43	11.90	0.18	0.29	0.37	0.56
Zr	17.60	1.56	2.49	1.35	2.00	0.95	13.80	0.53	0.41	0.67	0.50	0.21	0.59	0.57
Nb	9.68	0.25	0.07	0.03	0.39	0.10	0.83	0.04	0.02	0.31	0.02	0.01	0.01	0.01
Cs	4.93	0.11	0.07	0.04	0.09	0.03	0.31	0.01	0.01	0.03	0.01	0.02	0.01	0.01
Ba	565	26.70	125	13.80	473	7.69	23.20	22.90	2.86	30.50	4.33	3.14	91.50	4.80
La	17.20	4.71	2.26	0.91	0.54	2.10	2.22	0.16	0.78	3.10	0.06	0.11	0.12	0.19
Ce	34.30	7.50	3.94	1.47	0.95	3.60	3.62	0.32	1.44	6.52	0.12	0.17	0.22	0.36
Pr	4.22	0.89	0.45	0.15	0.10	0.43	0.39	0.03	0.17	0.90	0.01	0.01	0.02	0.03
Nd	17.30	3.51	1.78	0.65	0.44	1.93	1.45	0.16	0.86	4.32	0.06	0.09	0.11	0.18
Sm	3.14	0.71	0.38	0.12	0.08	0.53	0.26	0.07	0.24	1.61	0.01	0.03	0.02	0.05
Eu	0.98	0.46	0.24	0.05	0.03	0.57	0.12	0.03	0.21	1.28	0.01	0.02	0.01	0.04
Gd	2.64	0.66	0.38	0.11	0.08	0.56	0.24	0.07	0.26	1.63	0.01	0.03	0.04	0.05
Tb	0.45	0.11	0.07	0.02	0.01	0.13	0.04	0.01	0.06	0.41	0.01	0.01	0.01	0.02
Dy	2.15	0.57	0.35	0.08	0.05	0.78	0.22	0.08	0.38	2.27	0.02	0.05	0.07	0.07
Ho	0.38	0.10	0.06	0.02	0.01	0.14	0.04	0.01	0.08	0.44	0.01	0.01	0.01	0.01
Er	1.06	0.27	0.16	0.04	0.03	0.34	0.14	0.05	0.22	1.18	0.01	0.03	0.04	0.04
Tm	0.16	0.03	0.02	0.01	0.01	0.06	0.02	0.01	0.04	0.20	0.002	0.008	0.007	0.006
Yb	0.91	0.23	0.12	0.04	0.02	0.33	0.13	0.05	0.22	1.08	0.01	0.03	0.04	0.04
Lu	0.12	0.03	0.01	0.01	0.002	0.05	0.02	0.01	0.03	0.15	0.002	0.006	0.005	0.004
Hf	0.47	0.04	0.05	0.03	0.03	0.03	0.33	0.02	0.02	0.03	0.01	0.01	0.01	0.01
Ta	0.78	0.02	0.01	0.01	0.03	0.01	0.05	0.01	0.01	0.03	0.01	0.003	0.008	0.006
Pb	18.60	6092	1052	4689	11,871	592	/	/	165	579	251	/	544	/
Th	1.40	0.09	0.05	0.02	0.10	0.05	0.25	0.01	0.01	0.11	0.01	0.009	0.008	0.008
U	0.77	0.10	0.05	0.02	0.05	0.04	0.46	0.08	0.008	0.09	0.007	0.09	0.09	0.01
Eu/Eu*	1.02	2.05	1.94	1.51	1.05	3.14	1.53	1.58	2.61	2.90	2.19	1.60	2.26	2.39
Ce/Ce*	0.96	0.84	0.90	0.87	0.92	0.87	0.87	1.03	0.90	0.85	0.90	0.89	0.99	0.94
ΣREE	85.05	19.83	10.25	3.72	2.39	11.60	8.95	1.12	5.05	0.25	0.64	0.78	1.14	25.13
LREE	77.15	17.79	9.06	3.38	2.16	9.18	8.08	0.80	3.72	0.21	0.46	0.54	0.88	17.74
HREE	7.90	2.04	1.19	0.35	0.23	2.42	0.88	0.32	1.32	0.04	0.18	0.24	0.27	7.39
LREE/HREE	9.77	8.72	7.61	9.73	9.57	3.79	9.22	2.48	2.81	4.68	2.49	2.26	3.31	2.40
(La/Yb) _N	13.47	14.32	13.51	13.95	14.35	4.44	11.54	2.26	2.49	3.67	2.24	2.01	2.96	2.06
(La/Sm) _N	3.54	4.28	3.83	4.88	3.92	2.53	5.43	1.46	2.12	2.59	1.80	2.81	2.20	1.24
(Sm/Yb) _N	3.81	3.35	3.53	2.86	3.66	1.76	2.12	1.55	1.17	0.93	1.24	0.72	1.35	1.66

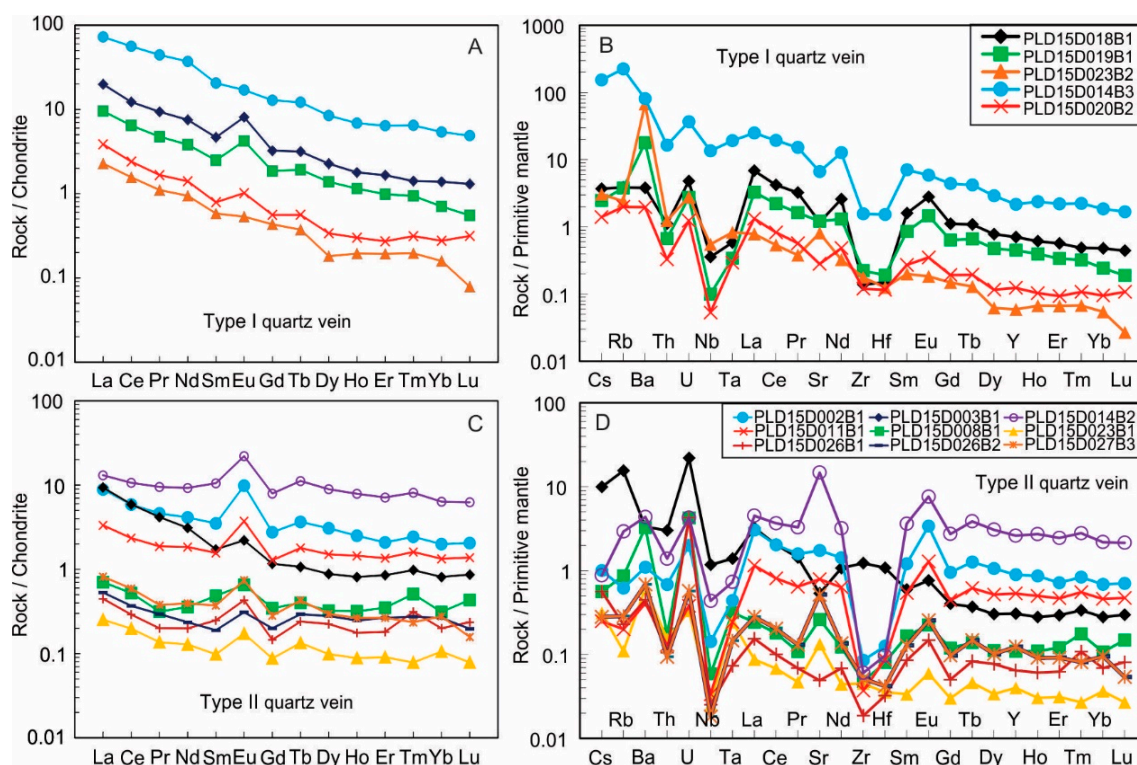


Figure 13. Chondrite-normalized REE patterns and primitive mantle-normalized trace-element patterns for the type-I and type-II quartz veins in the Pingliadian gold deposit. The chondrite- and primitive mantle-normalization data are from [55].

The Σ REE contents of biotite plagiogneiss, reddish alteration and sericite-quartz alteration were 41.71–79.77 ppm, 20.2–100.09 ppm, and 38.67–104.32 ppm (Table 2), respectively. These two types of rock were enriched in light rare earth elements (LREE), with LREE/HREE ratios of 13.79–15.45, 5.81–15.45 and 12.26–20.65, varying $(La/Yb)_N$ ratios of 23.48–31.13, 5.14–31.13 and 18.27–59.08 (Table 2), $(Sm/Yb)_N$ ratios of 5.2–5.44, 5.2–5.98 and 2.78–10.33, and $(La/Sm)_N$ ratios of 4.52–5.73, 2.88–5.73 and 4.43–7.23, respectively. Medium rare earth elements (MREE) were obviously depleted in these types of rock (Figure 12). These rocks showed moderately positive to weakly negative Eu anomalies (Table 2, Figure 12A,C,E), with Eu/Eu^* ratios of 1.08–1.34, 0.69–2.08 and 0.44–0.93 for biotite plagiogneiss and sericite-quartz alteration, respectively. The large ion lithophile element (LILE) contents in the biotite plagiogneiss showed moderate variations in Rb (19.6–53.3 ppm), Sr (248–382 ppm), and Ba (133–374 ppm), that's similar to the reddish alteration rock having Rb (14–49.4 ppm), Sr (138–303 ppm), Ba (102–228 ppm). Meanwhile, the sericite-quartz alteration rock had higher contents of Rb (97.6–174 ppm), Sr (9.97–84.7 ppm), and Ba (207–779 ppm) (Table 2). The concentrations of high field strength elements (HFSE) in the biotite plagiogneiss, reddish alteration and sericite-quartz alteration were 3.09–5.6, 2.23–19.8 and 1.52–8.44 ppm for Y; 0.69–0.97, 0.63–1.49 and 0.51–1.47 ppm for Hf; 4.49–1.94, 1.94–10.5 and 1.54–7.73 ppm for Nb; 0.235–0.78, 0.184–0.81 and 0.106–0.502 ppm for Ta; and 1.87–2.39, 0.764–4.94 and 2.03–4.37 ppm for Th, respectively. Nb, Ta, and Th were obviously depleted, whereas Y and Hf were slightly depleted (Figure 12B,D,F). The abundances of transition trace elements (TRTE) in these two rock types were 10.5–127 and 12.8–41.8 ppm for V, 2.72–23.1 and 2.24–8.87 ppm for Cr, 0.976–16.6 and 2.13–8.08 ppm for Co, and 1.39–24.3 and 1.62–6.44 ppm for Ni. Overall, the chondrite-normalized REE patterns showed negative Sm and positive Eu anomalies; however, primitive mantle-normalized spidergrams were characterized by negative anomalies of Cs, Ba, Th, Nb, Ta, Nd, and Ti, and positive K, Eu, and Gd peaks for these types of rock (Figure 12).

4.2.3. Geochemical Characteristics of the Two Types Quartz Veins

Trace elements were not remarkable in the two types of quartz veins in the Pingliidian gold deposit, a huge difference from the enveloped alteration halos. The Σ REE contents of the early and late quartz veins were very low: 2.39–85.05 ppm and 0.25–25.13 ppm, respectively (Table 3). The type-I quartz veins were relatively enriched in LREEs, with LREE/HREE ratios of 7.61–9.77, $(\text{La}/\text{Yb})_N$ ratios of 13.47–14.35, $(\text{La}/\text{Sm})_N$ ratios of 3.54–4.88, and $(\text{Sm}/\text{Yb})_N$ ratios of 2.86–3.81 (Table 3). The type-II quartz veins had low REE ratios, as mentioned above. Both types of quartz veins had similar MREE concentrations (i.e., Sm and Eu), although the chondrite-normalized REE patterns were quite different (Figure 13A,C), showing obvious depletion in all the rock types (Figure 13) and moderately positive to weakly negative Eu anomalies (Table 3, Figure 13A,C), with Eu/Eu^* ratios of 1.02–2.05 and 1.53–3.14 for the early and late quartz veins, respectively. The LILE contents were extremely high in the type-I samples 14B3 (short for PLD15D014B3) and 23B2 (short for PLD15D023B2) and the type-II sample 14B2 (short for PLD15D014B2), including 143 ppm of Rb in 14B3, 311 ppm of Sr in 14B2, 140 ppm of Sr in 14B3, 565 ppm of Ba in 14B3, and 473 ppm of Ba in 23B2. Meanwhile, the other two types of samples had low contents of these elements (Table 3), and Cs and Rb were generally depleted in primitive mantle-normalized spidergrams (Figure 13B,D). The Zr content was relatively high in the type-I quartz veins, ranging from 1.35 to 17.6 ppm, while that in the type-II quartz veins ranged from 0.209 to 0.956 ppm, except for sample 03B1 (13.8 ppm). The other HFSEs generally had low contents, but the Pb content was extremely high in both types of quartz vein. Nb, Th, Zr, and Hf were depleted in primitive mantle-normalized spidergrams, whereas U was enriched (Figure 13B,D). The variations in the TRTE concentrations were very unstable; the Zn and Cu contents peaked at 5059 ppm and 10,647 ppm, respectively, but also reached minimums of 1.49 ppm and 1.35 ppm (Table 3), respectively. The other TRTEs had similar trends to Zn and Cu, showing relatively low contents.

4.3. Mass-Balance Calculations

The quantitative calculation of the geochemical mass-balance in alteration zones and metasomatically transformed rock is compatible with mineral assemblages in reaction fronts that are associated with the main alteration [56]. The elemental gains and losses of the altered rock were calculated by the isocon method [57] (Figure 14), which was used to reveal the relative geochemical compositional changes that accompanied the alteration of the original rock (Figure 14A,B). Relatively immobile components (e.g., Al_2O_3 , TiO_2 , Sc, Zr) always showed coherent behavior during alteration [58]. We applied Grant's isocon method with Al_2O_3 as the immobile element to produce the following isocon equation [57]:

$$\Delta C_i = \frac{C_{\text{Al}_2\text{O}_3}^{\text{O}}}{C_{\text{Al}_2\text{O}_3}^{\text{A}}} \times C_i^{\text{A}} - C_i^{\text{O}}$$

Here, C_i^{O} and C_i^{A} are the concentrations of element component (i) in the original (O) and altered (A) sample, respectively. Thus, the gain or loss in wt % for major elements or in ppm for trace elements could be calculated from ΔC . The results are listed in Table 4.

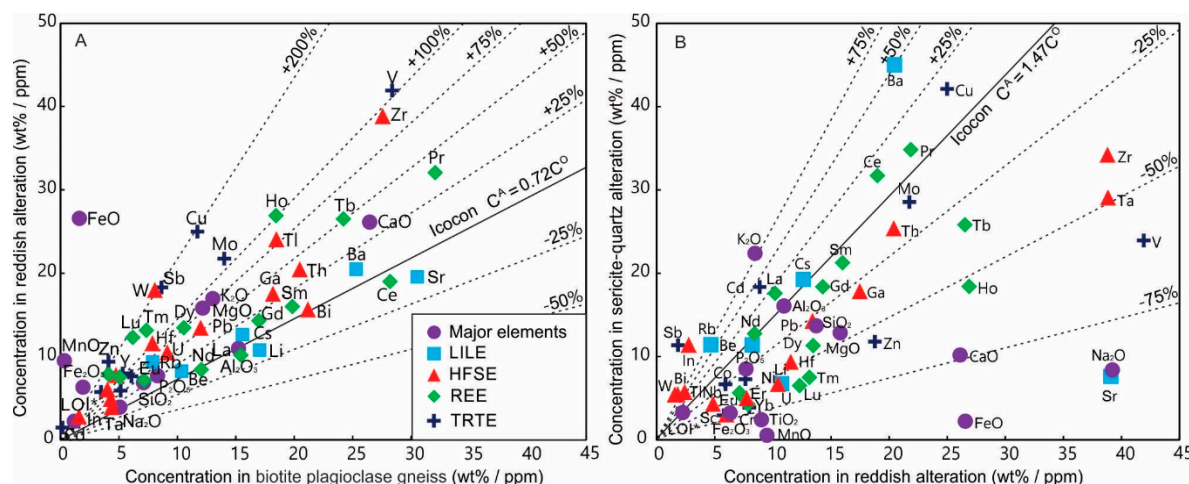


Figure 14. Isocon diagrams that show the elemental gains and losses of the altered rock (reddish alteration vs. the protolith biotite plagiogneiss and sericite-quartz alteration vs. the latest reddish alteration). The isocon lines are defined by the ratios of immobile elements (Al_2O_3), used to calculate the elemental gains and losses in the rock [57]. Enriched elements are above the isocon lines, while depleted elements are below the lines during alteration. Some elements are multiplied or divided by a constant (5, 10, 100, or 1000) to fit the diagram, which does not affect the validity of the mass-balance characteristics [57]. (A) Reddish alteration vs. biotite plagiogneiss. (B) Sericite-quartz alteration vs. reddish alteration.

Table 4. Calculated gains and losses from the isocon method for the average elemental contents in the two major alteration zones (except for abnormal samples 17B1 and 24B2).

ΔC_i	Reddish Alteration	Sericite-Quartz Alteration	ΔC_i	Reddish Alteration	Sericite-Quartz Alteration	ΔC_i	Reddish Alteration	Sericite-Quartz Alteration
SiO ₂	24.45	-21.94	Be	0.10	-0.04	Zr	26.34	-15.48
Fe ₂ O ₃	6.86	-4.12	Rb	25.487	31.21	Hf	0.81	-0.51
MgO	0.97	-0.70	Sr	-33.70	-169.51	Y	6.02	-4.33
CaO	0.98	-1.91	Cs	0.19	0.05	Pb	66.43	-36.99
Na ₂ O	0.38	-3.34	Ba	31.48	106.51	U	0.53	-0.58
K ₂ O	1.05	1.36	Sc	4.53	-3.73	Bi	0.005	0.21
MnO	1.28	-0.91	V	29.88	-25.59	Th	0.78	-0.31
TiO ₂	1.01	-0.73	Cr	5.77	-5.31	La	-1.28	1.82
P ₂ O ₅	0.02	-0.01	Co	3.09	-1.36	Ce	-1.80	2.63
LOI*	1.94	-0.003	Ni	4.55	-2.66	Pr	-0.16	0.18
FeO	35.31	-25.03	Cu	23.02	3.73	Nd	-0.32	0.26
F	0.60	-0.41	Zn	89.49	-53.67	Sm	0.24	-0.15
Cl	6.49	-38.70	Mo	0.16	-0.02	Eu	0.27	-0.32
S	45.19	-32.29	Cd	1.08	0.36	Gd	0.29	-0.17
Au	0.009	-0.003	Sb	0.16	0.59	Tb	0.12	-0.08
Ag	0.01	1.40	In	0.02	0.05	Dy	0.81	-0.57
As	-0.30	0.24	Ga	6.11	-5.34	Ho	0.18	-0.14
Hg	-0.38	3.47	W	1.68	1.92	Er	0.54	-0.41
B	4.06	3.16	Re	0.004	-0.004	Tm	0.10	-0.08
Li	-2.08	-6.15	Tl	0.14	0.14			

* LOI, loss on ignition.

5. Discussion

5.1. Mineral Dissolution and Precipitation Processes

The details of ore formation are always preserved within alteration halos. Such systems are geochemically open on a small spatial scale but closed on a larger scale [59]. Some evidences have been found in the Pingliidian gold deposit based on observed changes in the mineralogy aggregation and the bulk-rock geochemical compositions (Figures 5–10). The alteration and metasomatic transformation of

rocks are crucial characteristics of hydrothermal ore deposits [60], recording the details of ore formation through dissolution-precipitation mechanisms, with a sharp interface between the parent and product compositions in reaction fronts [20]. Reaction fronts where hydrothermal alteration occurs normal to fault cores in essentially unaltered wall rock can be easily recognized along regional-scale alteration zones of Mesozoic granitoids and Precambrian metamorphic rocks in Jiaodong. The compositions and textures in these reaction fronts before and after alteration represent the limits of ore-fluid infiltration and indicate the ore-formation process.

5.1.1. Early Alteration Stage

In the field, reaction fronts of reddish alteration can be easily recognized by the reddening of the rock from a hydrothermally altered granite because of the precipitation of hematite nano-platelets in pores [12,13,20,61] (Figure 3A,C,E,G,I). At the thin-section scale, the plagioclase and biotite in the Archean metamorphic rock were completely or partially replaced by K-feldspar, albite, muscovite, and quartz in the Pingliadian gold deposit (Figures 4 and 5). The textural relationships of the mineral assemblages intensively changed, as did their internal microstructures, with many brittle cracks forming. The original feldspars, generally clear and glassy in biotite plagiogneiss (Figure 4E,F), were replaced by turbid K-feldspar and albite, with massive porosity that was filled with nano-platelets of hematite and fluid inclusions [23] (Figure 5D–F). One of these replacement products, albite, had broader twinning striation than the original feldspar (Figures 4E and 5F). The presence of muscovite inclusions within feldspar is a significant indication that the replaced mineral overprinted another alteration (Figure 5D–F). The result of fluid interactions remained within the mineral assemblage, in which minor recrystallization with no significant changes in bulk–geochemical composition was also observed (Figure 5D–F).

The K_2O , Na_2O , and CaO contents were almost identical with the wall rock (Table 2, Figure 11A–C). The equilibration between the original and product feldspars likely accompanied cation exchange during fluid-induced phase separation, which strongly transformed the early feldspar's composition. The Fe_2O_3 and MgO contents decreased because of the consumption of biotite (Table 2, Figure 11D), except for the abnormal sample 17B1, which was enriched in Fe-bearing minerals. The variable TiO_2 and P_2O_5 contents were related to the breakdown or formation of accessory minerals, such as magnetite and apatite (Table 2). The LOI contents' increasing trend indicates that fluid flux increased. Thus, all the calculated major-element contents indicated gains, suggesting that the fluid was saturated in Fe and Si during the early alteration stage.

The ΣREE contents of reddish alteration were much lower than those of biotite plagiogneiss, except for two abnormal samples (17B1 and 18B4) (Table 2), which was a response to the mineral assemblage changing during the consumption of accessory titanite, monazite, zircon, and apatite. The abnormal data sets probably resulted from residual accessory minerals that were inherited from biotite plagiogneiss as inclusions in the feldspar. Most of the calculated REE contents indicated gains as high as 200% from the original to the product rock, except for La, Nd, and Ce loss (Figure 12). The biotite plagiogneiss was enriched in LREE (Table 2, Figure 12A), while the reddish alteration rock was relatively enriched in heavy rare earth elements (HREE, Table 2, Figure 12C), with lower LREE/HREE, $(La/Yb)_N$, $(Sm/Yb)_N$, and $(La/Sm)_N$ ratios than the biotite plagiogneiss. LREEs and MREEs were obviously depleted from the consumption of titanite and monazite (Figure 12). As mentioned above, LREEs and MREEs have higher mobility than HREEs during fluid–rock interaction, and the REE–rich minerals apatite and zircon gradually broke down because of increasing alteration intensity. The chondrite–normalized REE patterns showed obviously negative Sm and positive Eu anomalies. Moderately positive Eu anomalies (Table 2, Figure 12) with relatively high Eu/Eu^* ratios in reddish alteration were associated with Eu–rich feldspar minerals.

LILEs, such as Rb, Sr, and Ba, are enriched in biotite, plagioclase, muscovite, albite, and K-feldspar because of their preferential substitution of K^+ and Na^+ in the lattice of the original and alteration rock. The LILE contents of muscovite, albite, and K-feldspar in the product rock influenced the consumption

of biotite and plagioclase in the original rock, so the LILE contents exhibited gains and losses within $\pm 25\%$ of the original rock (Table 2, Figure 14A).

Y is found in apatite, while Hf, Ta, and Th are found in zircon and Nb in titanite. In the reddish alterations, Nb, Ta, and Th were depleted, and Y and Hf were slightly depleted in primitive mantle-normalized spidergrams (Figure 12). The consumption of these accessory minerals during accelerating alteration caused the gains in HFSE contents to contrast the losses in reddish alterations in the Mesozoic granite in the Sanshandao gold deposit [12] (Table 4, Figure 14A). Interpreting the exact reason for this abnormal situation is difficult. We suggest that the fluid flux rapidly dropped and the fluid dynamics became weak in the reaction fronts. Thus, these HFSEs remained in that area instead of migrating with the leaching fluid.

All the TRTEs increased in the reddish alteration rock (Table 4, Figure 14A). TRTEs were commonly concentrated in minerals such as biotite, magnetite, zircon, and hematite. Gains in Cu, Zn, and V exceeded the 100% isocon line because of the occurrence of minor disseminated sulfide during the early alteration stage (Table 4, Figure 14A). Cr, Co, and Ni preferentially appeared in nano-platelets of hematite when minerals such as biotite, magnetite, and zircon reacted with the fluid.

As mentioned above, the geochemical signatures of reddish alteration are consistent with changes in specific mineral assemblages as a response to various phase transitions from the relative roles of solid-state diffusion precipitation. A comparison of the Archean biotite plagiogneiss and reddish alteration rock compositions suggested that the bulk geochemistry was quite similar (Table 2, Figure 11), except for the abnormal sample 17B1, which consists of plagioclase or hematite phenocrysts. Even in a closed geochemical system, local mass transport must occur during the re-equilibration of rock [62]. Thus, the system may be chemically closed during reddish alteration, predominantly driven by changing P-T conditions during regional metamorphism. Minor fluid from metamorphic biotite in the parent gneiss accelerates the reaction.

5.1.2. Alteration that Was Related to Gold Mineralization

Representative sericite-quartz alterations were identified adjacent to auriferous quartz-vein orebodies in the field (Figure 3A–C,F–G,J, Figure 6A,B), which resulted from fluid-rock reactions overprinting the original reddish alteration rock. These alterations are characterized by reaction fronts with gray to dark-green color, consisting of massive sericite, chlorite, and epidote. Based on thin-section observations, the feldspar in the sericite-quartz alteration rock was definitely replaced by the sericite, quartz, muscovite, and sulfides that were observed in the typical hand specimens (Figure 6C–I). As evidence for the composition of the fluids during the reaction, the mineral assemblages and their textural relationships showed such reaction fronts (Figure 6E,F), which contained abundant porosity because of silica that was dissolved in the fluid. The reaction interface contains relict feldspars that are surrounded by disordered muscovite and fine laths of sericite mica (Figure 6E,F). The major minerals and their internal microstructures almost completely changed from the reddish alterations. Figure 6D shows typical cases, in which the crystallographic orientation was consistent with the foliation of the gneiss.

The bulk geochemistry significantly changed in the sericite-quartz alteration rock, related to the completely different alteration-mineral assemblage. Compared to the reddish alteration rock, the gains and losses are distinct compared to the original rock (Table 2, Figures 11, 12, and 14), including the abnormal sample 24B2, which is probably dominated by muscovite and sulfide phenocrysts.

The K_2O and LOI contents increased compared to those in the original rock (Table 2, Figure 11A,F), forming massive sericite and muscovite during the most intensive alteration and reaching equilibration with the fluid. However, the Na_2O and CaO contents decreased because of the complete consumption of feldspar, such as albite and K-feldspar (Table 2, Figure 6D,G, Figure 11B,C). Fe_2O_3 and Al_2O_3 had relatively stable contents compared to the Fe-bearing sulfide and Al-bearing clay (Table 2, Figure 6G–I, Figure 11D,E), indicating that Fe and Al were oversaturated in the ore-bearing fluid. The above accessory minerals were completely broken down, so the calculated TiO_2 and P_2O_5 contents

indicated loss and transportation by the fluid (Table 4). Generally, most of the calculated contents of the major elements indicated losses, especially SiO₂ and FeO (Table 4), showing that the properties of the fluid had completely changed.

On the contrary, the Σ REE contents slightly increased with the consumption of REE-rich accessory minerals in the sericite-quartz alteration rock. In fact, the LREE contents, especially La and Ce, were relatively high in the product rock (Table 2), forming new or preserving relict La- and Ce-rich monazite in the alteration rock. Thus, the LREE/HREE and (La/Yb)_N ratios were higher than those of the reddish alteration rock (Table 2), and the (Sm/Yb)_N and (La/Sm)_N ratios were relatively low. The chondrite-normalized REE patterns showed slightly negative Sm and positive Eu anomalies, except for sample 03B2 (Table 2, Figure 12). The Eu/Eu* ratios decreased because of the complete breakdown of feldspar in the sericite-quartz alterations. Most of the calculated REE contents indicated losses within -75% , while the LREE values indicated gains within $+25\%$ (Table 4; Figure 14B).

The LILE concentrations became complex in the sericite-quartz alteration rock because they are easily affected by the fluid behavior. The Sr content rapidly dropped because of the disappearance of feldspar (Table 2, Figure 12F), and Rb and Ba had extremely high contents because of their substitution of K, Na and Ca, exhibiting higher mobility during sericite-quartz alteration. Meanwhile, Cs, Ba and Sr were depleted in the chondrite-normalized REE patterns (Figure 12F), with an approximately 50% gain in Ba and over 75% loss in the calculated contents (Table 4; Figure 14B).

Most of the HFSEs were retained in the altered rock because of their low mobility. Nearly all the HFSEs, such as Nb, Ta, Ti, Th, Y, and Hf, were slightly to moderately depleted in the primitive mantle-normalized spidergrams (Table 2; Figure 12F). The Pb content was closely associated with the gold-hosting mineral galena, and Hf increased in the sericite-quartz alteration rock. Most of the HFSEs' calculated contents decreased, except for W, Bi, Tl, and In (Table 4; Figure 14B).

Some of the TRTEs (Cu, Cd, and Sb) were enriched, while others (Sc, Co, Ni, Zn, Mo, and V) exhibited decreasing calculated contents (Table 4, Figure 14B) because of the dissolution and precipitation of disseminated sulfides in the sericite-quartz alteration rock.

A sequential study of stable mineral assemblages, textural relationships, microstructures, bulk geochemistry and mass balances indicated that the sericite-quartz alteration rock formed from dissolution-precipitation reactions, which occurred at the reaction front as reddish alteration rock reacted with SiO₂⁻ and FeO⁻-bearing fluid (Table 4, Figure 6). Quartz, muscovite and minor pyrite precipitated with increasing metamorphic grades as fluid compositionally changed the affected system (Table 4; Figures 6 and 15).

5.1.3. Auriferous Quartz Veins and Gold Precipitation

The type II gray quartz veins in the Pinglidian gold deposit are virtual orebodies, in contrast to the type I milky quartz veins (Figure 7). As shown above, the type II auriferous veins precipitated at the center of the alteration zone and overprinted the type I quartz veins. The ore minerals were primarily pyrite and galena, followed by chalcopyrite and sphalerite, with minor pyrrhotite, freibergite, electrum, and native gold (Figure 8A–I).

Gold-hosting pyrites lack zoning in Pinglidian and are commonly cut by numerous brittle fractures (Figure 8D–F). Actually, these pyrites exhibited massive, ductile, single to interconnected, and linear to curvilinear distortions as lattice defects, and gold nanoparticles could also be present in the pyrite [13]. Pyrite and pyrrhotite corrosion textures are well developed because of replacement by galena (Figure 8G,H), including irregularly corroded interiors and concave margins. Pyrite precipitated slightly early, and then fluid-mineral reactions occurred, with galena changing the mineral textures and their assemblages during dissolution and precipitation.

The thin-section observations and electron probe microanalyses showed that the visible gold mainly occurred as inclusions in pyrite, microfracture fillings in pyrite, or inclusions along the margins of the sulfide grains [63] (Figure 8E, Figure 9A–D). SEM maps showed no zonation in terms of Au or Ag in electrum or gold, and other metals were not significantly present [13] (Table 1, Figure 9A,B). The

fine native-gold intergrowths with electrum probably formed by sub-solid exsolution (Figure 9A,B) during reactions with aqueous fluid. We did not consider the original source of gold during the above fluid-mineral reactions, so supersaturated gold-bearing solution was transported by the increasing Fe- and Pb-bearing fluid. The loss of H₂S and the destabilization of gold-bearing complexes is normally the most likely mechanism for gold precipitation [13,64–66]. Obviously, gold precipitation was associated with significant hydrothermal alteration, especially sericite-quartz alteration in the Pingliidian gold deposit (Figure 3A–C,F,G,J, Figure 6A,B). The dissolution-precipitation reactions between gold-bearing fluids and wall rock gradually decreased the solubility of the gold complex [Au(HS)²⁻], causing gold deposition [67]. Fluid-immiscibility processes are also used to interpret the mechanism of gold precipitation [68].

5.2. Physicochemical Conditions

As mentioned above, principal physicochemical parameters, such as fluid compositions (H⁺, Na⁺, and K⁺), temperature, pressure, pH, and *f*O₂, essentially control the processes of hydrothermal alteration and gold mineralization [12,69]. Although the details of these parameters are extremely complex and beyond the scope of the geologic problem in this paper, these simplified diagrams illustrate that this geochemical system corresponds to obvious changes in alteration mineralogy during hydrothermal processes. Numerous previous fluid inclusions of quartz showed homogeneous phase states at temperatures between 120 and 420 °C, particularly a range from 230 to 320 °C, with pressures of 78–300 MPa [49,68,70,71]. Brittle deformation occurred as fractures in the feldspar, and ductile deformation occurred as elongated quartz in the altered rocks (Figure 5B,C, Figure 6D–F), indicating that these microstructure deformations occurred at 300–400 °C [72–74]. We assume that local equilibrium was reached within the reaction front to precipitate the gangue–mineral assemblages because the temperatures varied (Figures 5D–F and 6D–F). Plümper and Putnis [69] calculated equilibrium constants to construct an activity diagram (H⁺, Na⁺ and K⁺) that related the fluid composition to K-feldspar, albite, and sericite in K–Na–Al–Si–O–H systems at 200 MPa and various temperatures (Figure 15). This situation is similar to that in the Pingliidian gold deposit, which could be applied to the reaction of gangue–mineral assemblages from 200 to 300 °C. During the early stage, plagioclases and biotite [K(Mg,Fe)₃AlSi₃O₁₀(F,OH)₂] were completely replaced by K-feldspar (KAlSi₃O₈), decreased aK⁺, and increased aNa⁺ in aqueous solutions, and the fluid compositions plotted in the stability field of K-feldspar and close to albite in the diagram (Figure 15). Then, both aK⁺ and aNa⁺ continuously decreased after K-feldspathization and albitization, during the fluid compositions entered the stability field of sericite (Figure 15). Textural observations, chemical analysis, and the calculated phase-equilibrium diagram suggested that albite and sericite predominantly formed intergrowths with each other, and occurred as contemporary alteration products during the early stage (Figure 5D,E, arrows 1 and 2). Sericite [KAl₂(AlSi₃)O₁₀(OH)₂] began to precipitate in the externally derived fluid as the temperature decreased, which shrunk the stability field of albite, favoring sericitization [69] (Figure 15). Thus, all the feldspars had completely transformed into sericite and quartz [75] (Figure 6D,E, arrows 1 and 2).

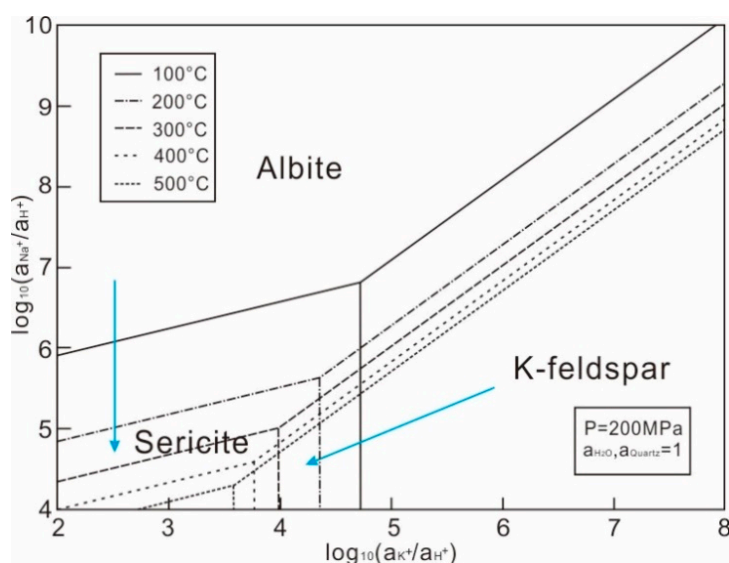


Figure 15. $\log(aK^+/aH^+) - \log(aNa^+/aH^+)$ diagram at various temperatures, 200 MPa and $a(H_2O) \times a(\text{quartz}) = 1$, which shows the stability field of K-feldspar, albite, and sericite. The diagram was produced by using equilibrium constants, and the thermodynamic data are from the slop98.dat database, as calculated by the SUPCRT92 program [76]. The arrow represents a possible decrease in K^+ and Na^+ , which caused the phase equilibrium of K-feldspar, albite, and sericite mineral assemblages.

Gold mineralization was closely related to sulfides and depended on the physicochemical conditions of the Fe-S-O-H system, as constrained by the fluid compositions (H_2S , HS^- , HSO_4^- , and SO_4^{2-}), temperature, pressure, pH, and fO_2 (Figure 16). Faure and Mensing [78] used sulfide-mineral pairs in equilibrium as a geothermometer, with fractionation errors of ± 40 – 50 °C. The $\delta^{34}S$ values of mineral pairs (pyrite: +9.5‰, galena: +6.2‰) from sample PLD15D016B1 indicated isotopic equilibrium at temperatures between 400 and 300 °C. Thus, the diagram was calculated for a Fe-S-O-H system (Figure 16), assuming a closed system and equilibrium conditions of 350 °C, 300 MPa, and $\Sigma S = 0.1$ mol/kg (the thermodynamic properties for $Au(HS)_2^-$ during the precipitation of ore minerals, especially sulfides [12,66,76] (Figure 16). Sulfide minerals such as pyrite, galena, pyrrhotite, chalcopyrite, and sphalerite were directly associated with gold precipitation in the Pingliadian gold deposit (Figures 7–10). The coexistence of these sulfide minerals was further constrained by the ore-forming fluid's composition, fO_2 , and pH [79] (Figure 16). Pyrite was the predominant gold-bearing mineral in the orebodies (Figure 8E, Figure 9C,D), and paragenetic pyrrhotite contacts pyrite and galena (Figure 8H). Furthermore, fO_2 was calculated to be between -23 and -35 in the stability field of the fluid compositions for pyrite and pyrrhotite (Figure 16). Gold was most likely transported as a gold-bisulfide complex below 350 °C rather than chloride [66]. Gold solubility contours [$Au(HS)_2^-$] were calculated in the diagram, which showed that the $Au(HS)_2^-$ concentrations occupied nearly the entire field of HS^- and H_2S , predominantly overlapping the stability field of pyrite and pyrrhotite (Figure 16). However, the solubility of $Au(HS)_2^-$ in the ore-forming fluid within the same area was sensitive to fO_2 along arrow 1 and the pH along arrow 2. This result suggests that an increase in fO_2 and a decrease in pH triggered gold precipitation in the assumed situation for the Pingliadian gold deposit.

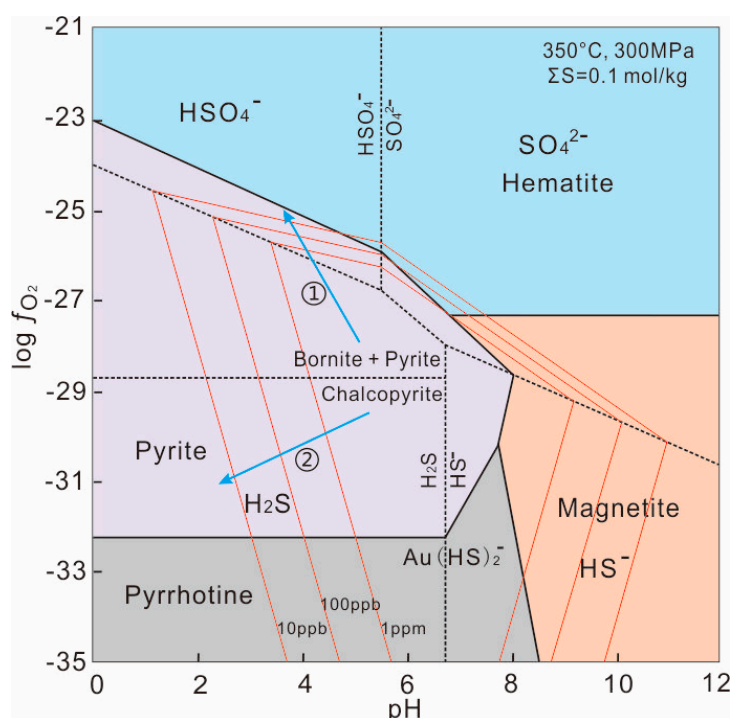


Figure 16. Log f_{O_2} –pH diagram at 350°C, 300 MPa, and $\Sigma S = 0.1$ mol/kg. The thermodynamic properties for $Au(HS)_2^-$ are from [77], and other data are from the slop98.dat database [12]. The narrow and bold lines represent the boundaries between aqueous sulfur species and Fe-bearing minerals, respectively. The calculated solubility contours of $Au(HS)_2^-$ at 10, 100, and 1000 ppb (thin continuous lines) are shown in the predominant fields of various aqueous sulfur species. The arrow represents a possible decrease in f_{O_2} and pH, which caused gold precipitation and the coexistence of sulfide assemblages.

5.3. Implications for Exploration

Once hydrothermal alteration has been identified, it can be directly related to the potential ore-forming fluid fluxes and scale of the host structures [8,10]. The detailed petrological features and geochemical effects of the Pingliidian gold deposit were presented above, providing vast quantities of information regarding the alteration-mineral assemblages and physicochemical conditions of the mineralizing fluids, which revealed that these ore-forming fluids interacted with the surrounding rocks in conjunction with gold mineralization [80]. These indicators of alteration zones increased the prospecting target, revealing that the structural control of auriferous quartz veins was paralleling to the foliation of the Archean metamorphic basement rock.

As mentioned above, the existence of an apparent positive correlation between the size of quartz veins and width of the alteration envelope in the Pingliidian gold deposit indicates that (1) quartz veins and alteration halos were controlled by foliations in fold belts that were overprinted by brittle-deformation structures (Figure 17A); (2) fluid circulation and fluid-flow movement along the quartz veins were prominently restricted to narrow conduits because of factors such as the porosity and permeability of the wall rock; (3) silica was supersaturated in the ore-forming fluids and interacted with large volumes of host rock by dissolution and precipitation, proven by gain and loss of major elements (SiO_2 , K_2O , Na_2O , and LOI), LREEs (La and Ce), MREEs (Eu), HREEs (Tm), LILEs (Rb, Ba, and Sr), HFSEs (Nb, Ta, Zr, and Hf) and TRTEs (Cu, Zn, Co, and Ni) (Figure 17B); and (4) equilibrium conditions existed in reaction fronts between the fluids and sub-solid rocks, with a sharp interface exchanging geochemical compositions (Figure 17B), as calculated above.

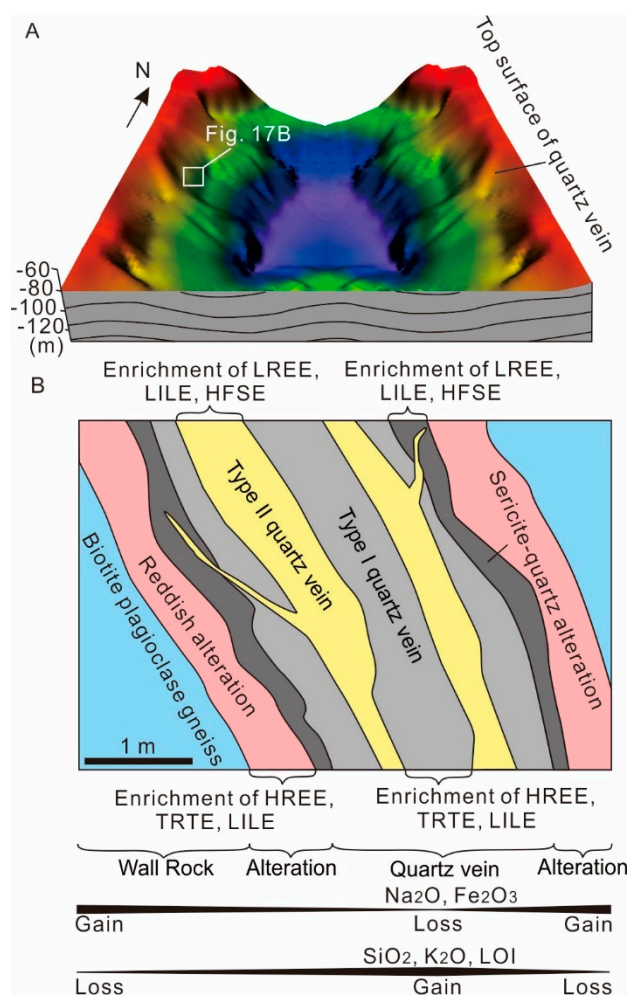


Figure 17. (A) Simulation of the ore-controlling structural pattern of the Pingliidian gold deposit, revealing depth variation of the top surface of inferred gold bearing quartz vein. (B) The geochemical indicator of two types quartz veins and their relationship to alteration rock and wall rock.

In contrast, an intensive 200-m-wide alteration zone in the footwall of the regional fault zone, including the Jiaojia Fault, Zhaoping Fault and Sanshandao Fault, is hosted in Mesozoic granitoids [12,81]. Second- and third-order faults from these fault zones exhibit negligible wall–rock alterations from the host structures, especially for the quartz-vein gold deposits (Linglong–type), but the hydrothermal reactions and gold mineralization are identical to the core of the alteration halo. Notable zonation is associated with the intensity of the alteration types from the fault core to wall rock, which depends on the permeability of the original wall rock. Fault cores or fault jogs are the pathways for fluid flow and the location for repeated deformation in fault zones [30], and these features have been proven to exhibit great potential for disseminated ores [7].

In summary, the geochemical loads of these altered mineral assemblages, alteration intensity, and range can be utilized to evaluate the potential size and scale of an ore-forming hydrothermal system under investigation, and thus is an effective exploration tool for estimating the structural deformation intensity decreased or increased in some degree in potential ore districts. These indicators reveal that the Archean metamorphic basement rock hosted auriferous quartz veins are structurally controlled by a local fault, which was parallel to the foliation of the biotite plagiogneiss.

6. Conclusions

(1) The Pingliadian gold deposit is hosted in Archean biotite plagiogneiss instead of Mesozoic granitoids. Gold mineralization was controlled by faults that are parallel to the foliations in the Archean biotite plagiogneiss. The orebodies consist of two types of quartz veins that are enveloped by intensive sericite-quartz alteration rock.

(2) Geological features and petrological observations showed clear spatial mineral-assemblage zonation from the infiltration of an external fluid during hydrothermal alteration, which produced auriferous quartz veins.

(3) The geochemical loads of these altered mineral assemblages displayed various concentrations of major elements (SiO₂, K₂O, Na₂O, and LOI), LREEs (La and Ce), MREEs (Eu), HREEs (Tm), LILEs (Rb, Ba, and Sr), HFSEs (Nb, Ta, Zr, and Hf) and TRTEs (Cu, Zn, Co, and Ni), which were preferentially enriched in specific minerals, especially sulfides and accessory minerals. The contents of these elements decreased as metasomatism increased during hydrothermal alteration.

(4) The re-enriched fluids triggered ore formation through a dissolution-precipitation mechanism, with a sharp interface between the parent and product compositions in the reaction fronts, causing the eclogitization of areas of the blueschist host that interacted with the passing fluid. Most of the original minerals were replaced, and the liberated Fe and Si were partitioned into the unsaturation fluid, thus precipitating the observed quartz veins and sulfides. More than 80% of the LILEs, REEs, and HFSEs were mobilized from the host rock as accessory minerals disappeared during intense alteration, with LILEs and LREEs mobilized more efficiently than HFSEs and HREEs. TRTEs mainly originated from the enriched fluid. The calculated sulfide-phase equilibrium showed that an increase in fO_2 and a decrease in pH caused gold precipitation in the assumed situation for the Pingliadian gold deposit.

(5) The petrological and geochemical indicators of the alteration zone increased the prospecting target and revealed the features of the structures that controlled the wall rock. The alteration intensity and range could be utilized to evaluate the potential size and scale of an ore-forming hydrothermal system, and thus represent an effective exploration tool for biotite plagiogneiss-hosted gold mineralization.

Author Contributions: Conceptualization, R.L.; methodology, R.L. and N.N.A.; formal analysis, M.Y.; investigation, Y.M.; data curation, M.Y.; writing—original draft preparation, R.L.; writing—review and editing, R.L. and M.Y.

Funding: This research was funded by the National Key Research and Development Program, Grant No. 2016YFC0600107–4; National Natural Science Foundation of China, Grant No. 41572069; National Key Research and Development Program of Deep-penetrating Geochemistry, Grant No. 2016YFC0600600 and National Nonprofit Institute Research Grant of IGGE, Grant No. AS2017J12.

Acknowledgments: We thank Li-Qiang Yang, Roberto Ferrez Weinberg, David Groves, and Richard Goldfarb for their assistance with this paper.

Conflicts of Interest: The authors declare no conflict of interest.

References

1. Tang, L.; Santosh, M. Neoproterozoic granite-greenstone belts and related ore mineralization in the north China craton: An overview. *Geosci. Front.* **2018**, *9*, 751–768. [[CrossRef](#)]
2. Li, S.R.; Santosh, M. Metallogeny and craton destruction: Records from the North China Craton. *Ore Geol. Rev.* **2014**, *56*, 376–414. [[CrossRef](#)]
3. Li, S.R.; Santosh, M. Geodynamics of heterogeneous gold mineralization in the North China Craton and its relationship to lithospheric destruction. *Gondwana Res.* **2017**, *50*, 267–292. [[CrossRef](#)]
4. Deng, J.; Wang, Q.F. Gold mineralization in China: Metallogenic provinces, deposit types and tectonic framework. *Gondwana Res.* **2016**, *36*, 219–274. [[CrossRef](#)]
5. Goldfarb, R.J.; Santosh, M. The dilemma of the Jiaodong gold deposits: Are they unique? *Geosci. Front.* **2014**, *5*, 139–153. [[CrossRef](#)]

6. Deng, J.; Wang, Q.F.; Li, G.J. Tectonic evolution, superimposed orogeny, and composite metallogenic system in China. *Gondwana Res.* **2017**, *50*, 216–266. [[CrossRef](#)]
7. Groves, D.I.; Santosh, M. The giant Jiaodong gold province: The key to a unified model for orogenic gold deposits. *Geosci. Front.* **2016**, *7*, 409–418. [[CrossRef](#)]
8. Bierlein, F.P.; Arne, D.C.; McKnight, S.; Lu, J.; Reeves, S.; Besanko, J.; Marek, J.; Cooke, D.R. Wall-rock petrology and geochemistry in alteration halos associated with mesothermal gold mineralization, central Victoria, Australia. *Econ. Geol.* **2000**, *95*, 283–312. [[CrossRef](#)]
9. Qiu, Y.; Groves, D.I.; Mcnaughton, N.J.; Wang, L.G.; Zhou, T. Nature, age, and tectonic setting of granitoid-hosted, orogenic gold deposits of the Jiaodong Peninsula, Eastern North China Craton, China. *Miner. Depos.* **2002**, *37*, 283–305. [[CrossRef](#)]
10. Mackenzie, D.J.; Craw, D.; Begbie, M. Mineralogy, geochemistry, and structural controls of a disseminated gold-bearing alteration halo around the schist-hosted bullendale orogenic gold deposit, New Zealand. *J. Geochem. Explor.* **2007**, *93*, 160–176. [[CrossRef](#)]
11. Pirajno, F. *Hydrothermal Processes and Mineral Systems*; Springer: Dordrecht, The Netherlands, 2009; pp. 1–162.
12. Li, X.C.; Fan, H.R.; Santosh, M.; Hu, F.F.; Yang, K.F.; Lan, T.G. Hydrothermal alteration associated with Mesozoic granite-hosted gold mineralization at the Sanshandao deposit, Jiaodong gold province, China. *Ore Geol. Rev.* **2013**, *53*, 403–421. [[CrossRef](#)]
13. Yang, L.Q.; Deng, J.; Wang, Z.L.; Guo, L.N.; Li, R.H.; Groves, D.I.; Danyushevsky, L.V.; Zhang, C.; Zheng, X.L.; Zhao, H. Relationships between gold and pyrite at the xincheng gold deposit, jiaodong peninsula, china: Implications for gold source and deposition in a brittle epizonal environment. *Econ. Geol.* **2016**, *111*, 105–126. [[CrossRef](#)]
14. Goldfarb, R.J.; Baker, T.; Dube, B.; Groves, D.I.; Hart, C.J.; Gosselin, P. Distribution, character and genesis of gold deposits in metamorphic terranes. In *Economic Geology 100th Anniversary*; Hedenquist, J.W., Thompson, J.F.H., Eds.; Society of Economic Geologists: Littleton, CO, USA, 2005; pp. 407–450.
15. Goldfarb, R.J.; Taylor, R.D.; Collins, G.S.; Goryachev, N.A.; Orlandini, O.F. Phanerozoic continental growth and gold metallogeny of Asia. *Gondwana Res.* **2014**, *25*, 48–102. [[CrossRef](#)]
16. Davies, J.H. The role of hydraulic fractures and intermediate depth earthquakes in generating subduction-zone magmatism. *Nature* **1999**, *398*, 142–145. [[CrossRef](#)]
17. Bons, P.D.; van Milligen, B.P. New experiment to model self-organize critical transport and accumulation of melt and hydrocarbons from their source rocks. *Geology* **2001**, *29*, 919–922. [[CrossRef](#)]
18. Faulkner, D.R.; Jackson, C.A.L.; Lunn, R.J.; Schlische, R.W.; Shipton, Z.K.; Wibberley, C.A.J.; Withjackd, M.O. A review of recent developments concerning the structure, mechanics and fluid flow properties of fault zones. *J. Struct. Geol.* **2010**, *32*, 1557–1575. [[CrossRef](#)]
19. Bons, P.D.; Elburg, M.A.; Gomez-Rivas, E. A review of the formation of tectonic veins and their microstructures. *J. Struct. Geol.* **2012**, *43*, 33–62. [[CrossRef](#)]
20. Putnis, A. Mineral replacement reactions. *Rev. Miner. Geochem.* **2009**, *70*, 87–124. [[CrossRef](#)]
21. Jamtveit, B.; Austrheim, H. Metamorphism: The role of fluids. *Elements* **2010**, *6*, 153–158. [[CrossRef](#)]
22. Arghe, F.; Skelton, A.; Pitcairn, I. Spatial coupling between spilitization and carbonation of basaltic sills in SW Scottish Highlands: Evidence of a mineralogical control of metamorphic fluid flow. *Geofluids* **2011**, *11*, 245–259. [[CrossRef](#)]
23. Parsons, I.; Lee, M.R. Mutual replacement reactions in alkali feldspars I: Microtextures and mechanisms. *Contrib. Miner. Petrol.* **2009**, *157*, 641–661. [[CrossRef](#)]
24. Skelton, A. Flux rate for water and carbon during greenschist facies metamorphism. *Geology* **2011**, *39*, 43–46. [[CrossRef](#)]
25. Jonas, L.; John, T.; King, H.E.; Geisler, T.; Putnis, A. The role of grain boundaries and transient porosity in rocks as fluid pathways for reaction front propagation. *Earth Planet. Sci. Lett.* **2014**, *386*, 64–74. [[CrossRef](#)]
26. Yang, L.Q.; Deng, J.; Wang, Z.L.; Zhang, L.; Guo, L.N.; Song, M.C.; Zheng, X.L. Mesozoic gold metallogenic system of the Jiaodong gold province, eastern China. *Acta Petrol. Sin.* **2014**, *30*, 2447–2467. (In Chinese)
27. Li, L.; Santosh, M.; Li, S.R. The ‘Jiaodong type’ gold deposits: Characteristics, origin and prospecting. *Ore Geol. Rev.* **2015**, *65*, 589–611. [[CrossRef](#)]
28. Lü, G.X.; Kong, Q.C. *Geology on the Linglong-Jiaojia-Type Gold Deposits in the Jiaodong Area*; Science Press: Beijing, China, 1993; pp. 1–253. (In Chinese)

29. Yang, L.Q.; Deng, J.; Wang, Q.F.; Zhou, Y.H. Coupling effects on gold mineralization of deep and shallow structures in the Northwestern Jiaodong Peninsula, Eastern China. *Acta Geol. Sin.* **2006**, *80*, 400–411.
30. Lu, H.Z.; Archambault, G.; Li, Y.; Wei, J. Structural geochemistry of gold mineralization in the Linglong-Jiaojia district, Shandong Province, China. *Chin. J. Geochem.* **2007**, *3*, 215–234. [[CrossRef](#)]
31. Deng, J.; Wang, Q.F.; Yang, L.Q.; Zhou, L.; Gong, Q.J.; Yuan, W.M.; Xu, H.; Guo, C.Y.; Liu, X.W. The structure of ore-controlling strain, stress fields in the Shangzhuang gold deposit in Shandong Province, China. *Acta Geol. Sin.* **2008**, *82*, 769–780.
32. Deng, J.; Yang, L.Q.; Gao, B.F.; Sun, Z.S.; Guo, C.Y.; Wang, Q.F.; Wang, P. Fluid Evolution and Metallogenic Dynamics during Tectonic Regime Transition: Example from the Jiapigou Gold Belt in Northeast China. *Resour. Geol.* **2009**, *59*, 140–152. [[CrossRef](#)]
33. Bierlein, F.P.; Crowe, D.E. Phanerozoic orogenic lode gold deposits. *Rev. Econ. Geol.* **2000**, *2000*, 103–139.
34. Wang, L.G.; Qiu, Y.M.; McNaughton, N.J.; Groves, D.I.; Luo, Z.K.; Huang, J.Z.; Miao, L.C.; Liu, Y.K. Constraints on crustal evolution and gold metallogeny in the northwestern Jiaodong Peninsula, China, from SHRIMP U–Pb zircon studies of granitoids. *Ore Geol. Rev.* **1998**, *13*, 275–291. [[CrossRef](#)]
35. Deng, J.; Wang, C.M.; Bagas, L.; Carranza, E.J.M.; Lu, Y.J. Cretaceous–Cenozoic tectonic history of the Jiaojia Fault and gold mineralization in the Jiaodong Peninsula, China: Constraints from zircon U–Pb, illite K–Ar, and apatite fission track thermochronometry. *Miner. Depos.* **2015**, *50*, 987–1006. [[CrossRef](#)]
36. Deng, J.; Yang, L.Q.; Li, R.H.; Groves, D.I.; Santosh, M.; Wang, Z.L.; Sai, S.X.; Wang, S.R. Regional structural control on the distribution of world-class gold deposits: An overview from the Giant Jiaodong Gold Province, China. *Geol. J.* **2018**, *3*, 1–14. [[CrossRef](#)]
37. Jahn, B.M.; Liu, D.Y.; Wan, Y.S.; Song, B.; Wu, J.S. Archean crustal evolution of the Jiaodong Peninsula, China, as revealed by zircon shrimp geochronology elemental and Nd-isotope geochemistry. *Am. J. Sci.* **2008**, *308*, 232–269. [[CrossRef](#)]
38. Wan, Y.S.; Dong, C.Y.; Xie, H.Q.; Wang, S.J.; Song, M.C.; Xu, Z.Y.; Wang, S.Y.; Zhou, H.Y.; Ma, M.Z.; Liu, D.Y. Formation Ages of Early Precambrian BIFs in the North China Craton: SHRIMP Zircon U–Pb Dating. *Acta Geol. Sin.* **2012**, *86*, 1447–1478. (In Chinese)
39. Wallis, S.; Enami, M.; Banno, S. The Sulu UHP Terrane: A review of the petrology and structural geology. *Int. Geol. Rev.* **1999**, *41*, 906–920. [[CrossRef](#)]
40. Tang, J.; Zheng, Y.F.; Wu, Y.B.; Gong, B.; Liu, X.M. Geochronology and Geochemistry of Metamorphic rocks in the Jiaobei terrane: Constraints on its tectonic affinity in the Sulu orogen. *Precambrian Res.* **2007**, *152*, 48–82. [[CrossRef](#)]
41. Zhou, X.W.; Zhao, G.C.; Wei, C.J.; Geng, Y.S.; Sun, M. EPMA U–Th–Pb monazite and SHRIMP U–Pb zircon geochronology of high-pressure pelitic granulites in the Jiaobei massif of the North China Craton. *Am. J. Sci.* **2008**, *308*, 328–350. [[CrossRef](#)]
42. Liu, P.H.; Liu, F.L.; Wang, F.; Liu, J.H.; and Cai, J. Petrological and geochronological preliminary study of the Xiliu ~2.1Ga meta-gabbro from the Jiaobei terrane, the southern segment of the Jiao-Liao-Ji Belt in the North China Craton. *Acta Petrol. Sin.* **2013**, *29*, 2371–2390. (In Chinese)
43. Deng, J.; Liu, X.F.; Wang, Q.F.; Dilek, K.; Yang, L.Q. Isotopic characterization and petrogenetic modeling of early cretaceous mafic dike–lithospheric extension in the North China craton, eastern Asia. *GSA Bull.* **2017**, *129*, 1379–1407. [[CrossRef](#)]
44. Yang, Q.Y.; Santosh, M. Early Cretaceous magma flare-up and its implications on gold mineralization in the Jiaodong Peninsula, China. *Ore Geol. Rev.* **2015**, *65*, 626–642. [[CrossRef](#)]
45. Yang, Q.Y.; Santosh, M.; Shen, J.F.; Li, S.R. Juvenile vs. recycled crust in NE China: Zircon U–Pb geochronology, Hf isotope and an integrated model for Mesozoic gold mineralization in the Jiaodong Peninsula. *Gondwana Res.* **2014**, *25*, 1445–1468. [[CrossRef](#)]
46. Zhang, J.; Zhao, Z.F.; Zheng, Y.F.; Dai, M.N. Postcollisional magmatism: Geochemical constraints on the petrogenesis of Mesozoic granitoids in the Sulu orogen, China. *Lithos* **2010**, *119*, 512–536. [[CrossRef](#)]
47. Ma, L.; Jiang, S.Y.; Dai, B.Z.; Jiang, Y.H.; Hou, M.L.; Pu, W.; Xu, B. Multiple sources for the origin of Late Jurassic Linglong adakitic granite in the Shandong Peninsula, eastern China: Zircon U–Pb geochronological, geochemical and Sr–Nd–Hf isotopic evidence. *Lithos* **2013**, *162*, 251–263. [[CrossRef](#)]
48. Yang, L.Q.; Deng, J.; Ge, L.S.; Wang, Q.F.; Zhang, J.; Gao, B.F.; Jiang, S.Q.; Xu, H. Metallogenic Age and Genesis of Gold Ore Deposits in Jiaodong Peninsula, Eastern China: A Regional Review. *Prog. Nat. Sci.* **2007**, *17*, 138–143.

49. Yang, L.Q.; Deng, J.; Zhang, J.; Guo, C.Y.; Gao, B.F.; Gong, Q.J.; Wang, Q.F.; Jiang, S.Q.; Yu, H.J. Decepritation Thermometry and Compositions of Fluid Inclusions of the Damoqujia Gold Deposit, Jiaodong Gold Province, China: Implications for Metallogeny and Exploration. *J. Earth Sci.* **2008**, *19*, 378–390.
50. Zhao, Z.; Zhao, Z.X.; Xu, J.R. Velocity structure heterogeneity and tectonic motion in and around the Tan-Lu fault of China. *J. Asian Earth Sci.* **2012**, *57*, 6–14. [[CrossRef](#)]
51. Sibson, R.H. Brittle failure mode plots for compressional and extensional tectonic regimes. *J. Struct. Geol.* **1998**, *20*, 655–660. [[CrossRef](#)]
52. Cox, S.F. The application of failure mode diagrams for exploring the roles of fluid pressure and stress states in controlling styles of fracture-controlled permeability enhancement in faults and shear zones. *Geofluids* **2010**, *10*, 217–233.
53. Cox, S.F.; Munroe, S.M. Breccia formation by particle fluidization in fault zones: Implications for transitory, rupture-controlled fluid flow regimes in hydrothermal systems. *Am. J. Sci.* **2016**, *316*, 241–278. [[CrossRef](#)]
54. Li, X.H.; Qi, C.S.; Liu, Y.; Liang, X.R.; Tu, X.L.; Xie, L.W.; Yang, Y.H. Petrogenesis of the Neoproterozoic bimodal volcanic rocks along the western margin of the Yangtze Block: New constraints from Hf isotopes and Fe/Mn ratios. *Chin. Sci. Bull.* **2005**, *50*, 2481–2486. [[CrossRef](#)]
55. Sun, S.S.; McDonough, W.F. Chemical and isotopic systematics of oceanic basalts: Implications for mantle composition and processes. *Geol. Soc. Lond. Spec. Publ.* **1989**, *42*, 313–345. [[CrossRef](#)]
56. Gresens, R.L. Composition-volume relations of metasomatism. *Chem. Geol.* **1967**, *2*, 47–65. [[CrossRef](#)]
57. Grant, J.A. The isocon diagram—A simple solution to Gresens equation for metasomatic alteration. *Econ. Geol.* **1986**, *81*, 1976–1982. [[CrossRef](#)]
58. Kishida, A.; Kerrich, R. Hydrothermal alteration zoning and gold concentration at the Kerr-Addison Archean lode gold deposit, Kirkland Lake, Ontario. *Econ. Geol.* **1987**, *82*, 649–690. [[CrossRef](#)]
59. Putnis, A.; John, T. Replacement processes in the Earth's Crust. *Elements* **2009**, *6*, 159–164. [[CrossRef](#)]
60. Cox, S.F.; Braun, J.; Knackstedt, M.A. Principles of structural control on permeability and fluid flow in hydrothermal systems. *Rev. Econ. Geol.* **2001**, *14*, 1–24.
61. Putnis, A.; Hinrichs, R.; Putnis, C.V.; Golla-Schindler, U.; Collins, L.G. Hematite in porous red-clouded feldspars: Evidence of large-scale crustal fluid-rock interaction. *Lithos* **2007**, *95*, 10–18. [[CrossRef](#)]
62. Carmichael, D.M. On the mechanism of prograde metamorphic reactions in quartz-bearing pelitic rocks. *Contrib. Miner. Petrol.* **1969**, *20*, 244–267. [[CrossRef](#)]
63. Du, X.J. Study on the technological mineralogy of the ores from the –145 level gold deposit of altered-rock type in Xincheng, Laizhou city. *Geol. Shandong* **1988**, *4*, 69–79. (In Chinese)
64. Huston, D.L.; Large, R.R. A chemical model for the concentration of gold in volcanogenic massive sulfide deposits. *Ore Geol. Rev.* **1989**, *4*, 174–200. [[CrossRef](#)]
65. Stefánsson, A.; Seward, T.M. Gold(I) complexing in aqueous sulphide solutions to 500 °C at 500 bar. *Geochim. Cosmochim. Acta* **2004**, *68*, 4121–4143. [[CrossRef](#)]
66. Williams-Jones, A.E.; Howell, R.J.; Migdisov, A.A. Gold in solution. *Elements* **2009**, *5*, 281–287. [[CrossRef](#)]
67. Wilkinson, J.J.; Johnston, J.D. Pressure fluctuations, phase separation, and gold precipitation during seismic fracture propagation. *Geology* **1996**, *24*, 395–398. [[CrossRef](#)]
68. Wang, Z.L.; Yang, L.Q.; Guo, L.N.; Marsh, E.; Wang, J.P.; Liu, Y.; Zhang, C.; Li, R.H.; Zhang, L.; Zheng, X.L.; et al. Fluid immiscibility and gold deposition in the Xincheng deposit, Jiaodong Peninsula, China: A fluid inclusion study. *Ore Geol. Rev.* **2015**, *65*, 701–717. [[CrossRef](#)]
69. Plümper, O.; Putnis, A. The complex hydrothermal history of granitic rocks: Multiple feldspar replacement reactions under subsolidus conditions. *J. Petrol.* **2009**, *50*, 967–987. [[CrossRef](#)]
70. Yang, L.Q.; Deng, J.; Guo, L.N.; Wang, Z.L.; Li, X.Z.; Li, J.L. Origin and evolution of ore fluid, and Au deposition processes at the giant Taishang Au deposit, Jiaodong Peninsula, eastern China. *Ore Geol. Rev.* **2016**, *72*, 582–602. [[CrossRef](#)]
71. Guo, L.N.; Goldfarb, R.J.; Wang, Z.L.; Li, R.H.; Chen, B.H.; Li, J.L. A comparison of Jiaojia-and Linglong-type gold deposit ore-forming fluids: Do they differ? *Ore Geol. Rev.* **2017**, *88*, 511–533. [[CrossRef](#)]
72. Scholz, C.H. The brittle-plastic transition and the depth of seismic faulting. *Geol. Rundsch.* **1988**, *77*, 319–328. [[CrossRef](#)]
73. Passchier, C.W.; Trouw, R.A. *Microtectonics*, 2nd ed.; Springer: Berlin, Germany, 2005; pp. 1–289.

74. Li, R.H.; Liu, Y.; Li, H.L.; Zheng, X.L.; Zhao, H.; Lu, H.W. Ore-controlling structure deformation condition of Xincheng gold deposit, Jiaodong: The microstructure and EBSD fabrics analysis constrain. *Acta Petrol. Sin.* **2014**, *30*, 2546–2558. (In Chinese)
75. Sverjensky, D.A.; Hemley, J.J.; D'Angelo, W.M. Thermodynamic assessment of hydrothermal alkali feldspar-mica-aluminosilicate equilibria. *Geochim. Cosmochim. Acta* **1991**, *55*, 989–1004. [[CrossRef](#)]
76. Akinfiev, N.N.; Zotov, A.V. Thermodynamic description of aqueous species in the system Cu–Ag–Au–S–O–H at temperatures of 0–600 °C and pressures of 1–3000 bar. *Geochem. Int.* **2010**, *48*, 714–720. [[CrossRef](#)]
77. Johnson, J.W.; Oelkers, E.H.; Helgeson, H.C. SUPCRT92: A software package for calculating the standard molal thermodynamic properties of minerals, gases, aqueous species, and reactions from 1 to 5000 bars and 0 to 1000 °C. *Comput. Geosci.* **1992**, *18*, 899–947. [[CrossRef](#)]
78. Faure, G.; Mensing, T.M. *Isotopes Principles and Applications*, 2nd ed.; John Wiley & Sons: New York, NY, USA, 2005; pp. 1–343.
79. Yang, L.Q.; Guo, L.N.; Wang, Z.L.; Zhao, R.X.; Song, M.C.; Zheng, X.L. Timing and mechanism of gold mineralization at the Wang'ershan gold deposit, Jiaodong peninsula, eastern china. *Ore Geol. Rev.* **2016**, *88*, 491–510. [[CrossRef](#)]
80. Rollinson, H.R. *Using Geochemical Data: Evaluation, Presentation, Interpretation*; Longman Publishing Group: New York, NY, USA, 1993; pp. 1–441.
81. Zhang, L.; Yang, L.Q.; Wang, Y.; Weinberg, R.F.; An, P.; Chen, B.Y. Thermochronologic constrains on the processes of formation and exhumation of the Xinli orogenic gold deposit, Jiaodong Peninsula, eastern China. *Ore Geol. Rev.* **2017**, *81*, 140–153. [[CrossRef](#)]



© 2019 by the authors. Licensee MDPI, Basel, Switzerland. This article is an open access article distributed under the terms and conditions of the Creative Commons Attribution (CC BY) license (<http://creativecommons.org/licenses/by/4.0/>).